CHARACTERISATION OF FLAME DEVELOPMENT WITH ETHANOL, BUTANOL, ISO-OCTANE, GASOLINE AND METHANE IN A DIRECT-INJECTION SPARK-IGNITION ENGINE

P.G. Aleiferis* and J. Serras-Pereira

Department of Mechanical Engineering, University College London, UK

D. Richardson

Jaguar Advanced Powertrain Engineering, Coventry, UK

*Author for Correspondence:

Dr. Pavlos Aleiferis

University College London

Department of Mechanical Engineering

Torrington Place, London WC1E 7JE, UK

Tel: +44-(0)20-76793862, Fax: +44-(0)20-73880180

E-mail: p.aleiferis@ucl.ac.uk

ABSTRACT

Research into novel internal combustion engines requires consideration of the diversity in future fuels that may contain significant quantities of bio-components in an attempt to reduce CO_2 emissions from vehicles and contribute to energy sustainability. However, most biofuels have different chemical and physical properties to those of typical hydrocarbons; these can lead to different mechanisms of mixture preparation and combustion. The current paper presents results from an optical study of combustion in a direct-injection spark-ignition research engine with gasoline, *iso*-octane, ethanol and butanol fuels injected from a centrally located multi-hole injector. Methane was also employed by injecting it into the inlet plenum of the engine to provide a benchmark case for well-mixed 'homogeneous' charge preparation. Crank-angle resolved flame chemiluminescence images were acquired and post-processed for a series of consecutive cycles for each fuel, in order to calculate in-cylinder rates of flame growth and motion. In-cylinder pressure traces were used for heat release analysis and for comparison with the image-processing results. All tests were performed at 1500 RPM with 0.5 bar intake plenum pressure. Stoichiometric (ϕ=1.0) and lean (ϕ=0.83) conditions were considered. The combustion characteristics were analysed with respect to laminar and turbulent burning velocities obtained from combustion bombs in the literature and from traditional combustion diagrams in order to bring all data into the context of current theories and allow insights by making comparisons were appropriate.

NOMENCLATURE

Da	Damköhler number
K	Karlovitz stretch factor
Ka	Karlovitz number
Le	Lewis number
Re_L	Reynolds number with respect to integral length scale
δ_l	Flame thickness
Ma	Markstein number
T	Temperature
P	Pressure
u'	Turbulence intensity
u'_k	Effective turbulence intensity
u_l	Laminar burning velocity
x, y	Co-ordinates
η	Kolmogorov microscale
τ_l	Timescale of laminar burning
τ_η	Timescale of turbulent straining
ϕ	Equivalence ratio

ABBREVIATIONS

AIT	After Ignition Timing
ATDC	After intake Top Dead Centre
CA	Crank Angle
COV	Coefficient Of Variation (=Mean/RMS)
DISI	Direct Injection Spark Ignition
EGR	Exhaust Gas Recirculation
EVC	Exhaust Valve Closure
EVO	Exhaust Valve Open
FFID	Fast Flame Ionisation Detector
IMEP	Indicated Mean Effective Pressure
IVC	Intake Valve Closure
IVO	Intake Valve Open
LIF	Laser Induced Fluorescence
MFB	Mass Fraction Burned
PFI	Port Fuel Injection
PIV	Particle Image Velocimetry
RMS	Root Mean Square
RPM	Revolutions Per Minute
SI	Spark Ignition
WOT	Wide Open Throttle

INTRODUCTION

BACKGROUND

Combustion of Alcohol Blends in Engines

Understanding the effect of biofuels on in-cylinder combustion processes is an essential challenge in managing fuel flexibility and achieving lower CO_2 emissions. Gasoline already contains 5% ethanol in many countries (E5) and can be compatible with existing engine fuel and combustion systems; however, its use will have limited impact on CO_2 emissions. Therefore, some markets are demanding much higher proportions, like E85, or even pure ethanol. The benefits of ethanol addition to gasoline have always been recognised for practical reasons. Apart from the variety of sources which it can be produced from, ethanol can raise the octane rating of gasoline due to its better anti-knock characteristics, allowing the use of higher compression ratios and higher thermal efficiencies. However, ethanol's high latent heat of vaporisation can cause problems for cold engine starting due to excessive charge cooling and poor evaporation [1]. On the other hand in hot climates ethanol fuelling can result in adverse effects such as vapour lock. Ethanol's water solubility and incompatibility with some engine materials are other disadvantages, hence compatibility issues with current fleet of vehicles and fuelling systems need to be resolved for high-content ethanol blends to become mainstream.

Combustion studies with ethanol in SI engines have been carried out by [2–7], focusing on performance characteristics, while others [8–11] have concentrated on engine emission measurements; most of these were done on Port Fuel Injection (PFI) engines. Very few studies have been conducted in latest technology Direct Injection Spark-Ignition (DISI) engines that are typically very sensitive to fuel properties; more to the point, in some of those studies, certain trends illustrate great diversity. For example, Zhu *et al.* [12] recently reported the combustion characteristics of a single cylinder SI engine with (a) gasoline PFI and DI, (b) gasoline PFI and ethanol DI, and (c) ethanol PFI and gasoline DI. The DI fuelling portion varied from 0–100% of the total fuelling, whilst the engine's air-to-fuel ratio was kept constant. It was shown that the indicated work output per unit volume (Indicated Mean Effective Pressure, IMEP) decreased by as much as 11% as DI percentage increased, except in case (b) where IMEP increased by 2% at light load. The combustion duration increased significantly at light load as DI fuelling percentage increased, but only moderately at full load (*i.e.* Wide Open Throttle, WOT). In addition, the percentage of ethanol in the total fuelling played a dominant role in affecting the combustion characteristics at light load; however, at full load the DI fuelling percentage became the important parameter, regardless of the percentage of ethanol in the fuel. Some of these findings are different to those of Aleiferis *et al.* [13] with PFI and DI fuelling which showed that DI increased the rate of heat release in general with both gasoline and gasoline/ethanol blends at low-load conditions. One reason for this discrepancy might be that Zhu *et al.* [12] used a low pressure multi-hole side injector with a nine-hole orifice plate at 20 bar injection pressure compared to the swirl-injector at 80 bar used in [13]. Although both injectors in these studies were side-mounted, the differences in injector types and injection pressures would lead to different atomisation mechanisms and different injection durations. Similar discrepancies have been found with centrally-mounted injectors run with gasoline and E85 [14]. Such comparisons illustrate the difficulties in drawing general conclusions from experimental data in the literature, especially when considering that changes in hardware and operating strategies can so easily change the outcomes of a test. This also highlights the importance of the injection system and its correct

4

optimisation, as well as the need for experiments under the same nominal conditions, in order to draw more confident conclusions when comparing the effects of a variety of fuels.

Butanol has also been suggested as a future fuel bio-component; it is more compatible with materials used in current fuelling systems but it has physical properties that can lead to poorer spray atomization. Butanol also lags behind ethanol in terms of commercial production. Butanol's performance has been studied less in the literature than ethanol's, even in PFI engines. Szwaja and Naber [15] showed marginally higher indicated efficiency for pure butanol fuelling and a faster 0–10% MFB period than that of gasoline in a PFI engine at 900 RPM with various engines loads. Engine stability (quantified by the Coefficient Of Variation of IMEP, COV_{IMEP}) was also marginally better for butanol. Other blends of butanol in gasoline showed that these effects were gradual with increasing volume fraction of butanol. Studies with PFI fuelling by Aleiferis and co-workers [16, 17] reported that addition of 25% butanol to *iso*-octane led generally to faster 0–10% MFB period than pure *iso*-octane fuelling, closer to gasoline's, and to better engine stability. However, trends were sensitive to equivalence ratio, spark timing, engine temperature and valve overlap. Very few studies on butanol combustion in DISI engines exist in the literature. Wallner *et al.* [18] studied the combustion performance of 10% ethanol and 10% butanol addition to gasoline in a 4-cylinder DISI engine. Data were taken at engine speeds in the range 1000–4000 RPM. Relatively minor differences were found between all three fuels in terms of heat release rate, 50% mass fraction burned, and COV_{IMEP} at low and medium engine loads. Pure butanol combustion data are relatively hard to find. Smith and Sick [19] studied *iso*-octane, ethanol and *iso*-butanol mixing and combustion with late injection strategy for stratified operation in an optical DISI engine and found that ethanol tended to ignite faster but otherwise burned similarly to the other fuels. Combustion phasing with *iso*-butanol was very similar to that of *iso*-octane, despite a longer ignition delay. Stable operation with the latter fuels was possible over a window of spark timing from 5–8° CA after the end of injection, whilst ethanol required an even narrower window of 5–7° CA.

Burning Velocities of Alcohols and Hydrocarbons

A major aspect of understanding combustion of alcohols in engines and decoupling some of the observed effects is the laminar and turbulent burning velocities of those fuels in a controlled environment at engine-like conditions. The laminar burning velocity has been measured for a range of hydrocarbon and alcohol fuels for various conditions by Gülder [20, 21], Metghalchi and Keck [22] and Bradley *et al.* [23] among others. More recently, results have been reported by Gu *et al.* [24] for methane, by Liao *et al.* [25] and Bradley *et al.* [26] for ethanol, by Al-Shahrany *et al.* [27] for *iso*-octane, by Jerzembeck *et al.* [28] for gasoline, by Gu *et al.* [29] and Sarathy *et al.* [30] for butanol, and by Beeckmann *et al.* [31, 32] for most of these fuels. A large database of fuel structure effects was also produced by Farrell *et al.* [33]; these authors reported data derived from thermodynamic analysis of the pressure rise from explosions in a combustion vessel (typically at 3 bar, 450 K), following the approach of Metghalchi and Keck [22]. However, their data were larger in absolute values than existing data for alkanes and aromatics by as much as 30% and the authors commented that this was due to use of different measurement techniques, *e.g.* thermodynamic (heat release) *vs.* optical (entrainment). This highlights more issues that can lead to differences between authors, *e.g.* flame cellularity effects at high pressure, method of deriving unstretched values of burning velocity, *etc.* Additionally, in most of the existing data, the effect of burned gas on the laminar burning velocity was not really quantified and hence very few data exist that would be more relevant to real engine conditions.

Typically, the overall effect of burned gas residuals on burning velocities has been found to be much greater than that of excess air, temperature or pressure. For example, with residual fractions of 0.15–0.2, the laminar burning velocity of *iso*-octane has been found to drop by 35–45% according to Metghalchi and Keck [22]. Such levels of residuals are commonly found in DISI engines at part-load operation and/or via Exhaust Gas Recirculation (EGR) to reduce NO_x. The recent work of Marshall *et al.* [34] presented laminar burning velocity measurements at engine-like conditions with and without residuals for various liquid fuels, including *iso*-octane and ethanol and discussed the effect of cellularity in comparison to the Metghalchi and Keck [22] data. Additionally, the recent work of Vancoillie *et al.* [35] presented a review of laminar burning velocity data for methanol and ethanol and new correlations for the operating range of alcohol-fuelled SI engines. Finally, very limited data exist on turbulent burning velocities at engine-like conditions in the literature. Lawes *et al.* [36] have published turbulent burning velocities for methane, *iso*-octane and Methanol, but no complete data really exist with presence of residuals and for longer chain alcohols at the exact same conditions for comparison. A recent study by Bradley *et al.* [37] presented turbulent burning velocities for ethanol at high temperatures and pressures.

PRESENT CONTRIBUTION

When one considers the need for fundamental understanding of in-cylinder processes with diverse fuels it is surprising that no major quantitative studies in the literature have compared in detail the in-cylinder behaviour of ethanol and butanol fuels in latest geometry DISI engines that have been designed originally to operate on hydrocarbons. Recent work by Serras-Pereira *et al.* [38, 39] demonstrated comparisons of in-cylinder spray formation and wall impingement with alcohols and hydrocarbons, along with some basic combustion data, using fuel injection in the early intake stroke for 'homogeneous' engine operation.

The main objective of the current work was to take a step further and characterise in detail the combustion process of *iso*-octane, gasoline, ethanol and butanol with early DI allowing maximum time for fuel evaporation, in comparison to that of gaseous methane in the same engine with PFI. Specifically, the paper presents measurements of speeds of flame growth and motion obtained by crank-angle resolved chemiluminescence imaging over a series of consecutive engine cycles with all fuels. Analysis of those data is done in conjunction with available in-cylinder flow data that have been obtained from an identical engine at the same operating conditions by Particle Image Velocimetry (PIV) [40]. Laser Induced Fluorescence (LIF) in the same engine has provided imaging of fuel concentration with a specially designed model fuel [41]. Considering the importance of in-cylinder ϕ at the spark plug location at ignition timing for all fuels, further LIF was considered. However, due to issues of quantification of the fuel concentration by LIF with such a diverse range of fuels, *e.g.* stemming from fluorescence quenching at different rates by the base fuels [19], it was decided to use *in-situ* Fast Flame Ionisation Detection (FFID) to measure the value of ϕ at ignition timing.

To the best of the authors' knowledge, this is the first time that such a complete set of data is presented for all these fuels in a latest geometry SI combustion system and it is believed that these measurements contribute towards a database of combustion rates which are essential for developing our knowledge of the underlying fundamental mechanisms under realistic engine conditions. The data can also assist modellers because simulation of combustion with various fuels at engine conditions can still be very challenging. Furthermore, one of the secondary – but still important – objectives of the current work was to collect

laminar and turbulent burning velocity data from the literature for all fuels and try to link in-cylinder observations to those velocities, as well as to traditional premixed combustion diagrams. This provided a framework for analysis and understanding in the context of both simplified combustion experiments and practical combustion systems running on 'standard' and 'future' fuels.

EXPERIMENTAL APPARATUS AND PROCEDURE

RESEARCH ENGINE

A single-cylinder research engine with optical access to the combustion chamber was used for the present work, as shown in **Fig. 1**. Optical access into the combustion chamber was possible via different configurations. For the current work, a traditional elongated hollow 'Bowditch' piston was used. An optical crown accommodating a 64 mm diameter quartz window was then screwed onto the piston so that a plan view of the combustion chamber was visible through a 45° mirror mounted within the hollow piston. The optical piston used three sets of rings made of Torlon® that allowed unlubricated running to prevent oil fouling the windows. The geometric parameters of the engine, as well as other system components are summarised in **Table 1.** The valve overlap on this engine resulted in levels of internal Exhaust Gas Residuals (EGR) of 15–20%. The air-to-fuel ratio was measured using a heated zirconia-based high-speed oxygen sensor (ECM© AFR Recorder 1200) installed in the exhaust manifold ~150 mm along the exhaust pipe from the engine head. The sensor allowed programming of the H-C and O-C ratios in order to accommodate different hydrocarbon and alcohol fuels. The ignition and injection timings were controlled using an AVL© 427 Engine Timing Unit (ETU) which generated crank-angle or time-based controlled trigger signals by receiving information from the engine's shaft encoders. This was also used for other engine-related control and synchronisation of signal sources and measurement systems (*e.g.* camera, in-cylinder pressure acquisition, *etc.*). More details about the engine and the test bed arrangement can be found in previous publications by the current authors [38, 39, 42].

FUELS

Five fuels were investigated: a typical commercial grade gasoline (RON95), *iso*-octane, ethanol, *n*-butanol (1-butanol), ethanol and methane. A standard commercial grade European gasoline contains several hundred hydrocarbons, typically about 25%–30% C5 or lower, 30%–40% C6–C8 and the remainder C9–C10 hydrocarbon chains. *Iso*-octane is a single component of gasoline with boiling point temperature of 99 °C at atmospheric pressure; *n*-butanol boils at 117°C while ethanol boils at 78.4°C. The distillation curve of the gasoline fuel is shown in **Fig. 2**. The boiling points of *iso*-octane, ethanol and butanol at 1.0 bar are shown in **Fig. 2** as vertical lines. The boiling points of the single components *n*-pentane and *o*-xylene have also been included in **Fig. 2** for reference purposes and in order to highlight two high and low volatility hydrocarbon components in gasoline, respectively. It should be noted here that *n*-butanol was selected for this study instead of its isomer *iso*-butanol because of the existence of some publications on the laminar burning velocity of *n*-butanol that could assist the analysis of the acquired data from the engine in direct comparison to the other fuels. However, *iso*-butanol is currently being studied in the same engine and results will be discussed in forthcoming publications in conjunction with some laminar burning velocity data for butanol's isomers that have been recently published [43].

INJECTOR

The fuel injection system used a prototype solenoid actuated Bosch[©] 6-hole injector with an asymmetric hole pattern as shown in **Fig. 3**. The nozzle-holes designated 3,4 were directed away from the spark-plug, pair 2,5 were targeted downwards into the cylinder and pair 1,6 were directed towards the spark-plug. For all work presented in this paper the DI fuel pressure was maintained at 150 bar. More details about the DI system can be found in [44, 45]. Methane was injected in the intake plenum using a Keihin[©] KN3-2 gas injector and 4 bar injection pressure. Typically, when injecting gaseous fuels with PFI some air is displaced by the gaseous fuel, leading to an in-cylinder charge with lower total energy than if the gaseous fuel had been injected with DI after intake valve closure. Therefore, sometimes researchers elect to adjust the throttle to account for the 'lost' air. Within the objectives of the current study it was deemed necessary to keep the same intake plenum conditions for all fuels in order to keep the in-cylinder flow nominally matched to that of the other fuels because any effect of engine load on the 'mean' and 'RMS' flow velocities at ignition could mask or exaggerate effects when comparing fuels. This issue has been carefully considered throughout analysis of the acquired data and more comments will be given in the results section.

OPERATING CONDITIONS

The baseline engine condition was set to 1500 RPM with 0.5 bar intake pressure. The influence of engine temperature on combustion was observed by using engine head and liner fluid cooling temperatures of 20 °C and 90 °C. The engine was run at stoichiometric and lean conditions with $\phi=1.0$ and $\phi=0.83$, respectively. The engine was mapped first in terms of IMEP and heat release analysis for spark advances in the range 50°–30° CA with all fuels [46]. A fixed spark advance of 35° CA was finally selected for visual characterisation of combustion for all fuels (*i.e.* ignition timing set to 325° CA ATDC). This corresponded to gasoline's Minimum spark advance for Best Torque (MBT) but it was close to MBT for all fuels as their IMEP response around that ignition timing was quite flat [46]. Using a fixed spark advance for all fuels allowed nominally same flow conditions at ignition timing; this will be discussed further in the results section. The injection strategy used a single injection event per cycle with timing set early in the intake stroke, 80° CA ATDC, to promote homogeneous mixture formation. The injection pulse widths used for stoichiometric operation are given in **Table 2** for all fuels.

IN-CYLINDER PRESSURE MEASUREMENTS

The in-cylinder pressure measurements for the present study were conducted with a water-cooled piezo-electric pressure transducer (Kistler[©] 6041A) connected to a charge amplifier (Kistler[©] 5011B10). The mean intake manifold pressure was recorded by a piezo-resistive transducer (Kistler[©] 4075A10) with its own amplifier (Kistler[©] 4618A0). A second absolute pressure transducer of the same type was mounted on the side of the cylinder 75 mm below the head gasket plane at the bottom of the cylinder barrel so that when the piston was close to bottom dead centre the pressure recorded could also be used for absolute in-cylinder pressure referencing.

The pressure signals were digitised at a sampling rate of 45 kHz on a cycle-to-cycle basis with a 12-bit analogue-to-digital converter (National Instruments[©] PCI-MIO-16E-4) within LABVIEW[®]. This rate corresponded to digitisation every 0.2° CA at 1500 RPM. The uncertainty due to electrical interference was a maximum of 0.05% of the full scale value for the in-cylinder pressure and 1% of full scale value for the intake plenum and barrel pressures, corresponding to an uncertainty of ±5.0 mbar and ±10 mbar, respectively. The pressure data were post-processed to calculate gross and net IMEP for each cycle,

amplitude and timing of peak in-cylinder pressure, including mean values and Coefficients of Variation (COV=Mean/RMS). Heat release analysis and calculation of Mass fraction Burned (MFB) was performed using methods based on [47, 48], following the practice of earlier work published by authors on the same engine for consistency [38–42]. The uncertainties involved in acquiring and processing in-cylinder pressure data were carefully considered. The error in numerical integration when calculating work output per unit volume (*i.e.* IMEP) can be minimised if the resolution is smaller than 1° CA [49]. Uncertainties can also arise from effects of signal noise, accurate definition of con-rod length and correct phasing of TDC with pressure [49]. The latter reference has reported ±2.5% uncertainty in IMEP given ±0.5° CA uncertainty in the phasing of TDC. In the current arrangement the accuracy of the con-rod length was accurate to below 0.01% and the position of TDC was accurate to within less than ±0.1° CA such that errors in IMEP and mass fraction burned due to experimental arrangements were considered negligible. A representative number of cycles for analysis was identified on the basis of COV_{IMEP} that achieved steady-state values at 150–200 cycles depending on conditions, hence 200 cycles were used for each test point analysis.

IN-CYLINDER EQUIVALENCE RATIO MEASUREMENTS

An HFR400 Cambustion© Fast-Flame Ionisation Detector (FFID) was used in order to quantify the fuel concentration at the spark-plug location at ignition timing for the different fuels. A detailed description of this instrument and its performance, as well as reviews of various applications and in-cylinder sampling, have been given by Cheng *et al*. [50]. The FFID has been found to respond with proportionality to alkanes, cyclo-alkanes, alkenes, alkynes and aromatic compounds with different number of C atoms in each molecule and the linearity of the instrument essentially means that the FID is generally conceived as a carbon counting device for hydrocarbons. The response function for other carbon-containing compounds has been shown to be different, however. For example, for alcohols and other compounds where carbon is already oxidised in the starting sample, an oxidised carbon fragment splits out in the endothermic cracking stage of the reactions, and this oxidised carbon fragment is incapable of producing ionisation in the flame [50]. Specifically for alcohols, the C bonded to O in the alkyl-O-H group contributes only to a fraction of a C atom. This is governed by the bond rupture process whether it occurs through the removal of the H atom (which does not produce ions) or the removal of OH (which does). The contributions of various bonds to the effective carbon number FFID response have been given in [50]; for pr   imary alcohols the effective contribution was 70% for ethanol and 85% for butanol. More details can be found in recent publications [51–54].

A spark-plug sampling kit supplied by Cambustion© was used to obtain in-cylinder samples next to the spark electrode (~1 mm). The main difficulty with the FFID technique applied to in-cylinder measurements is controlling the sample mass flow rate to the FID head, which pulsates substantially as a result of the range of pressures which the sample probe is exposed to. For intake and exhaust pressure measurements a constant pressure chamber is used between the sampling inlet and the FID detector itself, operated at below atmospheric pressure to act as a damping chamber and maintain a constant pressure across the feed tube to the FID chamber. For in-cylinder measurements however this is not enough; the flow resistance through the sample tube needs to be reduced further by using a smaller diameter tube of 0.008" and the constant pressure chamber volume must be increased substantially, which can be done by opening it to atmosphere *i.e.* infinite volume. All measurements refer to 'gaseous' fuel fractions; presence of liquid fuel, *e.g.* due to spark-plug electrode wetting at 20 °C, was likely to be different for each fuel but this was not measured by the FFID

instrument and the values of measured ϕ corresponded only to fuel vapour in the vicinity of the sampling probe. Further comments about this will be given in the results section.

Absolute uncertainties were very low, demonstrated typically by gaseous methane fuelling which produced a COV lower than 1% in the FFID signal plateau values. Cyclic variability in the FFID plateau signal level at the spark-plug location with the liquid fuels was ~10%. For comparison, the local mixture inhomogeneity measured by LIF in an engine of identical geometry by [41] has been found to be less than 10% on a scale larger than ~350 μm at ignition timing, hence quite small in relation to the integral length scale at that timing (~2 mm, as will be discussed later). Various duty cycles with firing and skip-firing were tested in order to examine and guarantee the integrity of the FFID signals (*e.g.* that the signal could reach its plateau value in all cycles). In the process, the difference between this signal levels and the firing levels also allowed estimation of the residual gas fraction. This was found ~0.15–0.2, in agreement with values calculated by modelling the engine's operation using geometrical and valve timing data via the methodology offered by [55].

FLAME IMAGING AND PROCESSING

A high-speed camera was used throughout the present study (Photron$^{©}$ APX-RS) to obtain images of flame growth. Typically a frame rate of 9 kHz was used, corresponding to 1 image/° CA at 1500 RPM engine speed (1 °CA = 0.111 ms). All images were digitised in 8-bit Tagged Image File Format (TIFF) files of 640×480 pixels resolution (corresponding to spatial resolution of 0.120 mm/pixel). All timings for images to be presented later refer to the falling edge of the triggering pulse, *i.e.* images at 3° CA refer to chemiluminescence acquired between 2° CA and 3° CA for a 1 image/° CA resolution.

In order to calculate the rate of flame growth and the directionality of flame motion for each fuel, 'enflamed' areas were obtained on a cycle-by-cycle basis via thresholding/binarisation of each flame image. Great care was exercised to define an appropriate circular region of interest on the flame images in order to isolate the flame only chemiluminescence without picking up light from reflections at the boundaries of the optical access. Mean flame growth curves were plotted for all fuels in terms of an equivalent radius calculated from the flame areas of all individual cycles based on a circle with the same area. This practice was elected as it provided data that could also be used for comparison with combustion bomb experiments where similar methods of quantification have been employed, *e.g.* [36]. The flame radius can reveal details very early in the combustion process (0–5% MFB), a period that is not typically resolved well by thermodynamically derived MFB data. The temporal derivative of flame radius was also calculated to enable quantification of flame growth speed. Uncertainties in the calculated ensemble averaged flame area were carefully estimated by considering binarised flames. The area calculated for a flame was compared to the area of the same flame with an extra pixel added to the equivalent flame radius. This was considered to represent an uncertainty linked to the spatial resolution of the imaging arrangement. Secondly, the change in the binarised area of a flame due a change in the threshold value was also computed. For very small flames at ~10° CA after ignition (1–2 mm depending on ϕ, with almost 0% MFB identified from heat release analysis) these uncertainties were found to be ±9% and ±0.2–0.4% per threshold unit of the nominal equivalent flame radius, respectively. For larger flames ~30° CA after ignition (~5–10% MFB, depending on ϕ), when considering a wider window of uncertainty of 10 pixels, the uncertainties were still quite low, ±0.5–2% and ±1–2% of the equivalent flame radius, respectively.

The geometric centroid of area for each flame was identified in *x* and *y* image co-ordinates and calculated for the duration of flame growth. The centroid co-ordinates were used to plot the displacement of the flame from the spark plug (hence the flame-centroid motion path), along with the rate of change of that displacement, *i.e.* the flame's centroid speed. For the latter it was considered useful to employ different measures of flame centroid speed, a 'global' one more biased towards 'bulk' motion and 'local' one which allowed analysis of effects along the path of the flame-kernel's motion, as will be explained in detail in the results section.

RESULTS AND DISCUSSION

CHARACTERISTICS OF HEAT RELEASE

The mean in-cylinder pressure traces and associated curves of MFB are shown for all fuels in **Figs. 4–7** for ϕ=1.0 and 0.83 and for both 20 °C and 90 °C engine coolant temperatures. For 20 °C the highest in-cylinder peak pressure was achieved by ethanol followed by methane, then butanol and gasoline with very similar values, and finally *iso*-octane with clearly the lowest; categorisation was the same for IMEP. Similar trends were found for the phasing of various percentages of MFB, with ethanol exhibiting the fastest combustion; however, butanol showed an overall faster MFB than gasoline (positioned between methane and gasoline), the result of which is also visible in the slightly more advanced timing of peak pressure obtained relative to gasoline. Cyclic variability in IMEP and peak pressure was in the range 2–4% amongst fuels, with ethanol exhibiting the lowest values and *iso*-octane the highest. At 90 °C, butanol and ethanol showed almost identical peak pressure, with butanol exhibiting faster MFB, especially after TDC (*i.e.* 35° CA After Ignition Timing, AIT). *Iso*-octane was yet again clearly the slowest of the fuels, with methane faster than gasoline in the early stages of combustion and slower after TDC. Cyclic variability decreased to levels of 1.5–2% at 90°C with very small differences between fuels.

At lean conditions (ϕ=0.83) in **Figs. 6–7**, methane at 20 °C exhibited very similar peak pressure, IMEP and MFB to that of ethanol, but at 90 °C it was clearly slower than ethanol, but of very similar burning rate to that of butanol at the same conditions throughout the combustion process. Gasoline and *iso*-octane were both slower than all the other fuels; it is also worth noting that *iso*-octane produced the lowest IMEP at 20 °C. Overall, the timing of 10% MFB was retarded by about 5 °CA for all fuels in comparison to stoichiometric conditions. Cyclic variability in IMEP was in the range 4–10% at 20 °C and 3–5% at 90 °C, with the alcohols more robust to changes in fuelling than the liquid hydrocarbons.

The rate of pressure rise associated with compression reveals details about the levels of charge cooling for different fuels. It was clear that between 300–325° CA ATDC, *i.e.* well after intake valve closure but before ignition timing, the in-cylinder pressure was higher with methane than those of the liquid fuels for both 20 °C and 90 °C (despite not adjusting the engine load for methane to account for air displacement). Amongst the liquid fuels there was very little difference, however. Given the higher latent heat of evaporation of both ethanol and butanol relative to *iso*-octane and gasoline, one might have expected the alcohols to have exhibited much higher levels of charge cooling overall, hence quite lower temperature and pressure at ignition timing in comparison to the hydrocarbons. Close analysis of the pressure-volume diagrams and polytropic indices showed that differences in pressure amongst all liquid fuels were typically smaller than ~0.05 bar and in temperature smaller than ~10 K. For comparison, methane's pressure at ignition timing was ~0.2 bar higher than those of the liquid fuels at 90 °C and ~0.1 bar at 20 °C; this translated to ~25 K higher

11

temperature at ignition timing for methane. These differences have been taken under consideration in the discussion later in this paper and further comments will be made on potential effects where relevant.

Analysis of data from evaporation modelling and wall heat flux measurements with the exact same liquid fuels by [39], and from charge cooling measurements with various oxygenated blends using a cold wire resistance thermometer by [51], indicated that the higher levels of charge cooling during injection with alcohol fuels can result in gradual reduction in the evaporation rate overall because the latter can be limited by fuel saturation due to the higher mass injected and/or by diffusion and mixing. Saturation in temperature drop during injection has also been measured optically by Beyrau *et al.* [56]. In an identical engine to that of the current study, the overall effect of saturation was a temperature difference between gasoline and ethanol at the spark-plug location at ignition timing of only ~8 K [51], *i.e.* well in agreement with what quoted earlier.

CHARACTERSTICS OF FLAME GROWTH

General Observations

An example of typical flame growth for all fuels is shown in **Fig. 8** with engine coolant temperature 20 °C. Growth was fastest with ethanol, then butanol and methane, followed by gasoline and *iso*-octane. This was similar to that obtained from the MFB curves, except for methane. Ethanol and butanol showed high flame luminosities in the initial and late combustion stages followed by gasoline, *iso*-octane and methane. Alcohol flames and methane flames had noticeably different visual characteristics, both in terms of overall transparency and internal structure than *iso*-octane or gasoline flames. The former produced more 'spatially homogeneous' intensity flames where the 'flame fronts' appeared cloudy and less luminous, exhibiting lower contrast within the flame and a less wrinkled, textured appearance. More specifically, methane flames were quite 'clean', *i.e.* they displayed very uniform intensity levels across the flame area, with virtually no spikes observed on the image intensity histogram and a smooth gradient of intensity into and out of the flame. At the other extreme, gasoline and *iso*-octane flames had a more clearly defined flame front or 'flame brush'. It is not currently known where these visual characteristics stem from, hence flame spectroscopy has been planned and results will be discussed in a future publication in conjunction with regulated and unregulated exhaust emissions (*e.g.* aldehydes, see [53] for an interesting analysis on the latter).

The 'probability of flame presence' is presented in **Fig. 9** for all fuels. These contours were obtained by averaging the binarised flames of all cycles for each fuel; the lower limit of the scale (black) represents 0% probability, whilst the upper (red) 100%. A timing of 25° CA AIT was used for this figure to demonstrate differences between fuels at the development stage where the largest flame size was observed (for ethanol) just before 'masking' effects by the piston crown window started to affect the derived flame contours and quantities; the white circle illustrates the boundaries of the optical crown. The images are shown for 20 °C where the largest differences were observed between fuels, as well as the largest displacement from the spark plug were recorded. Overall all flames showed preferable motion towards the exhaust side of the combustion chamber. However, there were differences between the fuels; for example, while methane flames were quite 'circular', those of butanol showed a larger degree of variability, not only in flame size but also in flame shape/distortion due to the particular directionality of motion/growth of this fuel, which appeared to be more biased towards the east side of the combustion chamber. This effect is believed to stem from butanol's poorer atomisation during injection and subsequent impingement of spray plumes 1 and 6 onto cylinder liner,

especially for cold engine conditions [38]. More detailed characterisation of the observed patterns of flame growth and motion are discussed in the next sections.

Flame Radius

The flame growth radius is given in **Fig. 10** for 20 °C and 90 °C. To put those graphs into context with the earlier discussion, flames were typically 'clipped' by the boundaries of the optical piston crown window from ~25–30° CA AIT onwards (especially for the faster fuels) and this is the reason why the flame radius growth slows down after that timing in **Fig. 10** and eventually saturates at a maximum value that corresponds to the radius of the optical crown that defined the size of optical access. In order for the reader to remain alerted about this, a vertical dotted line has been drawn in the graphs of **Fig. 10** at 25° CA AIT.

In an attempt to provide a link between the flame growth data derived by image processing and the MFB data derived from in-cylinder pressure measurements, the equivalent flame radius was used to estimate an average enflamed volume on the basis of an equivalent sphere. For a flame radius of 12–15 mm, which corresponded on average to 25–30° CA AIT, the mass fraction burned calculated from the enflamed volume was found to be of the order 5–10% using appropriate values of density for the unburned and burned mixtures calculated from [57]. This agrees with the MFB data shown earlier in **Fig. 5** and further highlights the usefulness of optical observation during the first 30° CA following ignition timing, which could provide insights into combustion phenomena during the initial flame kernel development stage very early on in the cycle (0–5% MFB) where MFB data derived from in-cylinder pressure traces are typically subject to the highest inaccuracies due to the low level of pressure rise above the motoring pressure.

The radius of flame growth showed that the alcohols burned faster than the hydrocarbon fuels in the early flame kernel development stage. In particular butanol was observed to have an early flame growth very similar to ethanol at 20 °C which was not demonstrated in the MFB data. At 20 °C methane had the lowest values of flame size in the 0–20° CA AIT period. After ~25° CA AIT though, methane flames showed a rapidly growing flame radius which was similar to gasoline's, clearly accelerating in rate of growth, hence switching over to the same trend observed between methane and gasoline in the MFB data of **Fig. 5**. The effect was also reflected in the COV of methane's flame radius which was double that of the other fuels at 15° CA AIT and only matched the COV of the other fuels at ~25° CA AIT. It was also noted that although methane's radius did not reach that of butanol even at ~30° CA AIT, the rate of growth in flame radius was higher than that of butanol as will be discussed in more detail later. This suggests that the behaviour of methane early in the cycle (*i.e.* at MFB less than 5–10% as picked up by the imaging data) was indeed quite different to that later in the cycle (*i.e.* at timings greater than 10–20% MFB as picked up by the in-cylinder pressure measurements).

At 90 °C engine coolant temperature, the trends between fuels were similar to those at 20 °C, but differences in flame sizes between fuels were smaller. Butanol at 90 °C showed high-luminosity early flame kernels during the 0–15° CA AIT period (*i.e.* during the overlap with the spark discharge). The flame growth period 15–25° CA AIT showed ethanol growing marginally faster than butanol. Methane was again initially slow but the COV of flame radius had reduced markedly from that at 20 °C and matched that of the other fuels as early as 15° CA AIT. Methane also had higher flame growth rate than gasoline, while *iso*-octane exhibited the slowest flame growth of the group. In general at 90 °C, the trends in flame radii early on in the cycle, *i.e.* for MFB<5–10%, were very similar to those observed by the MFB curves obtained from in-cylinder pressure

measurements for MFB>5–10%, hence all fuels had consistent behaviour from ignition timing to combustion completion when the engine was fully warm.

Flame Growth Speed

The flame growth speed is shown in **Fig. 11**. Ethanol and butanol showed higher values of speed than the liquid hydrocarbon fuels; while methane showed an initial lag in growth, its later rate of growth was very similar to the alcohols. The earliest stage of combustion, 0–15 °CA AIT, exhibited faster acceleration which could be related to the spark event as it is likely that this contributed a certain degree of assistance to the expansion of the initial flame kernel. After ~10–15° CA AIT the flames showed slower acceleration. The difference between these two earlier and later values is clearer at 90°C for all fuels. The values of flame growth are shown up to 24° CA AIT as after 25° CA AIT they carry quantitatively no direct relevance to fuel properties since they were affected by limitations in optical access; however, for completeness it may be noted that the values started to drop after about 28–30 °CA AIT with similar gradients for all fuels till ~50° CA AIT when the optical bore had been filled by the flame for all fuels and flame growth values dropped down to zero level.

When the flame growth speed was plotted as a function of flame radius in **Fig. 12**, the data for all fuels fell on top of each other in the very early stages of flame growth but showed clear separation over the main phase of observed flame growth from 3–15 mm. The alcohols and methane exhibited largest measured values of ~13 m/s, whilst *iso*-octane was the slowest at ~10 m/s; clearly the largest flame speeds were recorded at 90° C.

A measure of flame stretch rates was calculated for all fuels from the equivalent flame radius and flame growth speed on the assumption of the stretch that would be experienced by a sphere, $(2/R)(dR/dt)$; this is shown in **Fig. 13**. At ignition, the initial kernel is highly stretched for all fuels and a minimum level of spark energy must be supplied to establish a self-sustained kernel (this amount depends on ϕ and is typically ~0.25 mJ for gasoline). The measured levels of stretch during the first 10–15° CA (*i.e.* for flame radii smaller than 1–2 mm) were quite variable and overlapping amongst fuels, but once the flame kernels had become self-sustained after that very early stage, clearer separation was observed. At 20 °C, stretch was initially highest for methane, then ethanol, butanol and finally *iso*-octane, followed very closely by gasoline. Stretch values converged to similar levels for all fuels at ~20–25° CA AIT (or close to ~15 mm in radius). At 90 °C, *iso*-octane and gasoline still produced very similar stretch rates while ethanol's became separated from methane; butanol produced very similar stretch rates to the liquid hydrocarbons. For comparison, and in order to put the numbers in **Fig. 12** in perspective, experiments in combustion 'bombs' have shown extinction stretch rates for methane at atmospheric pressure and temperature of ~1700 s^{-1} at ϕ=1 and ~500 s^{-1} for *iso*-octane; hence stretch rates in the engine are much higher. This issue will be discussed further with respect to Markstein numbers in later sections.

Turbulent Burning Velocities

Lawes *et al.* [36] measured turbulent burning velocities for *iso*-octane, methane and methanol from explosions by Schlieren imaging in a combustion bomb at 5 bar and 358 K with u'=2 m/s and 20 mm integral length scale. Values of ~0.9 m/s and 1.2 m/s were reported for *iso*-octane and methane flames, respectively, at 30 mm radius (*i.e.* 3 times the integral length scale in diameter). It was also reported that turbulent burning velocities were approximately 3–4 times the corresponding laminar burning velocities.

To compare the engine flames of the current work with the turbulent burning velocities of Lawes *et al.* [36], the flames had to be compared at sizes scaled by the difference in integral length scale. The integral length scale in the engine was calculated following the methodologies of Fraser and Bracco [58] who found that the longitudinal integral length scale (in the cylinder axis) scaled with the clearance height by ~0.1–0.15 from 310°–360° CA ATDC in the compression stroke. Using the instantaneous cylinder volume from 300°–360° CA ATDC from the current engine, an 'equivalent' clearance height was calculated by dividing by the cylinder bore area, from which an integral length scale could be obtained. These scales were calculated to be ~3 mm at 300° CA ATDC reducing to ~2 mm at ignition timing and ~1.2 mm at TDC. Interestingly, the PIV measurements of Rimmer *et al.* [40] in an identical engine to that of the current study at the same operating conditions showed that the greatest influence on combustion came from frequencies in the range ~250–600 Hz. For measured velocities of ~2 m/s inside the pent-roof at 300° CA ATDC, those frequencies correspond to eddy sizes of 3–8 mm, *i.e.* broadly in agreement at the smallest scale with the estimates derived at 300° CA ATDC based on the work of Fraser and Bracco [58].

Considering an integral length scale of ~2 mm in the engine, flames with sizes in the range 2–6 mm had to be used to calculate burning velocities from the measured flame growth speeds, therefore flames with radius close to ~3 mm were considered appropriate as they corresponded to a size ~3 times the integral length scale. The ratio of unburned to burned gas densities was then used to obtain an estimate of the turbulent burning speed by dividing the measured flame growth speed by this ratio; it was calculated by [58]. It should be noted that this ratio remains nearly constant over most of the combustion event and this is a useful property because it simplifies the analysis [59].

Using this approach on the engine data of **Fig. 12** at 90 °C, values of 0.86 m/s and 1.24 m/s were calculated for *iso*-octane and methane, respectively. These values are quite close to the values of Lawes *et al.* [36] (~0.95 m/s and ~1.3 m/s, respectively). Turbulent burning velocity data for the exact same type of gasoline used in the current study were also made available from Sheppard and Lawes [60] and given as ~1.05 m/s at stoichiometry; the value calculated from the engine flames was 1.02 m/s. Ethanol and butanol burning velocities were 1.1 and 1.02 m/s, respectively, for which immediate comparison was only possible with that of methanol, ~1.45 m/s, in the study of Lawes *et al.* [36]. However, the work of Bradley *et al.* [37] showed recently turbulent burning velocities for ethanol in the bomb at the same conditions of [36], *i.e.* 358 K and 5 bar, but for ϕ=0.9 and 1.1 and flame radii in the range 50–100 mm. The values deduced from their graphs and averaged over the two equivalence ratios was ~1.65 m/s at flame radius of 50 mm, *i.e.* at a flame size 5 times the integral length scale in the bomb. Therefore, comparison with the data from the engine was done at a flame radius of 5 mm; the value calculated was 1.35 m/s.

Considering that the temperature and the pressure in the bomb were ~12% lower and 33% higher, respectively, than in the engine, the overall effect if those conditions transferred to the engine would be a decrease of about 25–30% in laminar burning velocity in the engine (the higher percentage decrease would apply to methane due to the slightly higher temperature and pressure at ignition timing than the liquid fuels from lack of charge cooling effects as discussed earlier); see subsequent section on laminar burning velocities for details. The presence of residuals in the engine leads to about 35–40% decrease in laminar burning velocity [22, 34]. Therefore, the net effect would be an increase in laminar burning velocity in the engine at the conditions of the bomb of ~10%. Furthermore, considering the values of ϕ at the spark plug

location at ignition timing measured by FFID for all fuels, summarised in **Table 3**, the slightly leaner values recorded for *iso*-octane and gasoline (than the nominal ϕ=1.0), suggest a further 5% decrease in laminar burning velocity, therefore, when combined with the 10% increase, it would lead to a net effect of ~5% increase in laminar burning velocity at most. For completeness it may also be said that other differences between the engine data and the combustion bomb may be stemming from potential existence of sub-micron size fuel droplets in the mixture field close to spark plug at ignition that could affect the burning rate; however, the effect should be small (~5%) at the turbulent intensity levels of the engine, especially in the early flame development stage, as has been documented recently by combustion-bomb experiments with *iso*-octane aerosols [61].

Taking all the aforementioned scale factors under consideration, the turbulent burning speeds in the engine would have been about 5–10% larger than those calculated from **Fig. 12** if at the conditions of the bomb as a best approximation for all fuels. Considering that the turbulent burning velocities for methane, *iso*-octane and gasoline were ~4 times larger than the laminar values at stoichiometry [36], and for ethanol about 5–6 [37], this would translate almost to the exact differences in turbulent burning velocities seen above between engine and combustion bomb. Such an agreement between a modern SI engine and the controlled experiment of a combustion bomb at carefully scaled conditions is noteworthy. Obviously, the burning rates in the engine continue to increase further during combustion because the flames grow to ~30–40 times the integral length scale before reaching the walls. A comparison between the ethanol flame growth speeds in the engine with the ethanol burning data of Bradley *et al.* [37] at flame sizes of 10 integral length scales reveals a reasonable agreement between engine and combustion bomb. Specifically, the turbulent burning velocity increases by a factor ~1.6 when the flame grows from a size of 5 integral length scales to 10 in the bomb, whereas in the engine the respective factor is ~1.35. Effects from large-scale 'mean' flow and anisotropy in the engine on flame sizes larger than ~3 integral length scales may be linked to such difference; the next section will discuss in-cylinder flow effects on the flame's motion in detail. Therefore, the engine data can be quite useful for relative quantification of flame speeds with all fuels both within and beyond the length-scale limits of combustion bombs; *e.g.* the current data revealed that butanol was slower than ethanol by about 8% but faster than gasoline by about 5%, a useful result when considering the absence of detailed turbulent burning velocity data for butanol from combustion bombs.

CHARACTERISTICS OF FLAME MOTION

The effect of the in-cylinder flow on the early flame kernel growth can be distinguished by two main attributes: large-scale convection by 'bulk' flow motion and smaller scale effects by 'turbulence'. In reality, it is very difficult to decouple these effects reliably (if not at all), especially on a crank-angle-resolved cycle-by-cycle basis. The flame 'sees' increasing number of sizes and frequencies of turbulent length scales as it grows; those scales that are larger than the size of the kernel will primarily 'convect' it without distortion (*e.g.* away from the spark-plug electrodes), whilst those smaller than the kernel will distort and/or wrinkle it depending on the degree of turbulence. The flame centroid displacement calculated from images can thus be used as an indication of the motion of the flame kernel due to flow effects, particularly during its early growth. The centroids of flame areas were calculated for all cycles and the extracted average flame centroid co-ordinates were plotted for each crank angle and for each fuel to show how the flames were displaced from the spark-plug electrode from as early as 3° CA AIT to 50° CA AIT, as shown in **Fig. 14**. The (0, 0) point

represents the spark-plug electrode tip as superimposed schematically on the flame motion paths. The end points were the same for all test cases as they were directly equivalent to the centre of the optical piston crown, and resulted as the flame 'aligned' itself with the centre of the bore during completion of the combustion process.

The flame centroid displacement paths in **Fig. 14** demonstrated quantitatively how all flames grew primarily towards the exhaust side of the chamber first before expanding into the intake side. PIV in the engine [40] showed that the mean flow field at ignition timing was nearly symmetrical between the left and right-hand-side of the combustion chamber (*i.e.* west and east of the spark plug), with a central 'channel' of flow running from the intake to the exhaust side, hence it is believed that the initial directionality of the flame's motion was a result of this. However, it was interesting to note that the different fuels were associated with different flame-centroid paths on average. Methane was used as a benchmark fuel to represent flame growth in a fully homogeneous fuel concentration field, and as such the flame motion was considered to be affected mainly by the flow field. This was confirmed because the flame path of methane was not really affected by changes in the engine temperature, as shown in **Fig. 14** for 20 °C and 90 °C (the change in engine coolant temperature does not really affect the directionality of the in-cylinder flow motion at ignition timing [63]). In contrast, there were clear differences between the paths of motion for the liquid fuels at 20 °C and 90 °C. Specifically, at 20 °C, ethanol had a longer flame centroid path than gasoline and butanol; *iso*-octane showed similar flame centroid displacement pattern to ethanol *albeit* skewed towards the right-hand side of the combustion chamber (*i.e.* to the south-east side of the spark plug). It further appeared that groups of fuels with high boiling points exhibited flame centroid displacements in similar directions, *i.e. iso*-octane and butanol, whilst ethanol (with a boiling point somewhere in the middle of the distillation curve of gasoline) followed a path more akin to gasoline. The bias towards the right-hand side of the combustion chamber at 20 °C may be associated with the directionality of spray plumes 1 and 6 that showed worse atomisation and higher levels of impingement on that side of the liner wall at 20 °C engine temperature, primarily for the fuels with high boiling points [38, 39]. The effect was not replicated at 90 °C which suggested that there were different mechanisms involved, related primarily to better evaporation and mixing for all fuels. The increased levels of evaporation and, therefore, degree of mixture homogeneity (under the early injection strategy used) would bias the sensitivity of flame motion more towards the local velocity flow field, over the fuel concentration field. This would explain the greater similarity of the flame motion for all fuels at 90° C, particularly when considering that their paths of motion were shifted closer to methane's.

In order to add a temporal dimension to the trends shown in **Fig. 14**, the change in 'centroid distance' from the spark plug with time, *i.e.* from the (0, 0) point, was plotted in **Fig. 15**. This centroid distance quantified the initial movement of the flames towards the exhaust side of the engine and the subsequent change of direction towards the intake side. Broadly speaking, this figure shows that the flames moved relatively uniformly away from the spark plug in the period from 0–30° CA AIT, although not necessarily in the same directions. The first inflection point after ~25–30° CA AIT corresponded to the start of masking effects on the flame contours by the optical crown and then to rapid change in direction of flame propagation from the exhaust side of the combustion chamber towards the intake side and, therefore, back towards the spark plug. In order for the reader to remain alerted about this, a vertical dotted line has been drawn in the graphs of **Fig.**

15 at 25° CA AIT. The second inflection point around 40° CA AIT resulted as the flame centroid moved past the spark-plug electrode towards its final co-ordinates at the centre of the combustion chamber.

Fig. 15 also shows that whereas for 20 °C there was a relatively wide range between 25–30° CA AIT for flame reversal to occur, at 90 °C this range became smaller, reflecting the similarities in flame location characteristics at high temperatures where differences in mixture preparation effects should be reduced. Values of largest flame displacement from the spark-plug location before any flame masking took place ranged between 4.5–6.5 mm (equivalent to 15–20% of the optical crown radius) at 20 °C, but were more uniform for all fuels at 90 °C (5.5 mm, or ~17% of the optical crown radius). The centroid of methane flames did not move far away from the spark plug and its path was much shorter than the other fuels at 90 °C. Butanol at 20 °C also exhibited limited motion away from the spark plug, lower than methane's and lower by ~20% when compared to *iso*-octane that moved the furthest; this may be associated with the mixture preparation of butanol at cold conditions as also mentioned earlier and described in more detail in [38, 39].

For completeness, the cumulative average flame centroid path length throughout the cycle is plotted in **Fig. 16**. Ethanol appeared to have the longest flame centroid path in time, with gasoline and butanol close behind. Methane was in the middle at 20 °C but exhibited behaviour more akin to ethanol and butanol at 90 °C. Relative to the speed of combustion however, the results indicated that the distances the flame travelled around the combustion chamber did not appear to determine the quality of the combustion. On the other hand when this parameter was plotted *versus* flame size in **Fig. 17**, it appeared that fuels that had the highest boiling points (*iso*-octane and butanol) also had the lowest cumulative centroid displacements, especially at 20 °C. At hot conditions most fuels behaved similarly in this regard.

The similarities at 90 °C between the two alcohols in **Figs. 14–16** may suggest that the longer fuel injection durations that were required for alcohol fuelling might have influenced the flow field at ignition timing due to prolonged momentum exchange with the fuel spray during injection early in the cycle. To examine potential effects, the PIV study of Rimmer *et al.* [40] was carefully considered. These authors found that a single injection event of 1 ms duration per cycle in the early intake stroke (same strategy to that of the current study) produced ~10% lower RMS velocity at ignition timing than a 'split' injection strategy with three sequential injection events of 0.3 ms duration each early in the intake stroke; the effect of an injection strategy with two sequential injection events led to 5% increase in RMS velocity at ignition timing. However, the differences in RMS between the different strategies just 10 °CA AIT had dropped levels below 4–5%. Considering that the higher RMS results from 'perturbing' the intake flow valve jet for a longer period of time during the injection process using the multiple spray shots (~25° CA in total including opening and closing time between shots, in comparison to ~9°CA for the single injection strategy), as well as the differences in the injection duration for the different fuels in **Table 2**, it is plausible that differences in the flow at ignition timing with the different fuels could exist, but these would be of similar magnitude to those measured in [40], *i.e.* 5–10%.

A measure of flame centroid speed, termed 'global', was calculated by dividing the displacement vector from the spark-plug at any crank angle by the time elapsed after ignition at that crank angle. As such it represented a centroid speed biased towards 'bulk' motion and it essentially filtered the effects of local smaller-scale flow effects. **Fig. 18** illustrates that the global flame centroid speeds were quite similar across fuels, typically in the range 1.0–2.5 m/s. This magnitude is close to the 'mean' in-cylinder flow velocities measured in [40];

specifically, a dominant cross flow from the intake to exhaust sides of the chamber was reported by those authors, exhibiting a mean value of 2.0 m/s 25° CA before ignition timing, increasing to approximately 2.8 m/s 20° CA AIT; velocities as low as 1.5 m/s were recorded on a cycle by cycle basis.

By calculating the change in flame centroid displacement with time via a 'finite difference' approach, the 'local' flame centroid speed was also obtained from **Fig. 14**, revealing previously masked effects of smaller flow scales on flame motion, especially at the early stages of flame growth. This relationship is shown in **Fig. 19**. The early flame growth phase of 0–20° CA AIT was characterised by large changes in the local displacement speeds, with all fuels showing generally similar trends, particularly at 90 °C. 'Local' flame centroid speeds exhibited values as high as 3–4 m/s throughout 10–20° CA AIT, reducing down to levels of ~1–1.5 m/s at about 25° CA AIT; this was the timing where the flame contour started to get gradually 'clipped' by the limitations in optical access for the fastest burning flames. The smaller peak values early on in the combustion process at 90 °C for all liquid fuels are again consistent with methane's behaviour, which points to the flame-centroid speed being a better representation of the magnitude of flow velocity at higher engine temperatures due to better fuel evaporation and mixing, hence a weaker effect from differences in fuel concentration, as discussed in more detail earlier. The plots of 'local' flame centroid speed versus flame radius in **Fig. 20** show that, although the flames of different fuels behaved similarly, some of these were subjected to different levels of 'straining' by the in-cylinder flow. For example, the flames of *iso*-octane and butanol exhibited ~0.5–1 m/s lower centroid speed than the other fuels when growing from 5 to 15 mm in radius, hence associated with different levels of flame strain overall.

REGIMES OF COMBUSTION

Laminar Burning Velocities

One of the difficulties in using laminar burning velocity data lay in finding the data at the same temperature and pressure conditions for different fuels. However, in an attempt to make use of current knowledge on burning velocities in relation to a practical combustion system, data from studies at conditions of high temperature and pressure relevant to SI engines at ignition timing were collected and are given in **Table 4** for all fuels used in the current study at ϕ=1.0 and 0.8; velocities at 1.0 bar have also been included for completeness and reference. This table, although result of a quite thorough survey, may not be exhaustive and further efforts should continue to bring more/new data into a single database. Some researchers have derived mathematical relationships to fit their data and allow calculation of values at pressures and temperatures typical of SI engines over a wide range, typically 1–8 bar and 300–700 K. These are of the form of a power law and show that there is much greater temperature sensitivity than pressure sensitivity [22, 24, 34].

One of the observations in **Table 4** is that the laminar burning velocities at high pressures show small differences for the liquid fuels, typically much smaller in comparison to those observed between the fuels at atmospheric conditions. More to the point, at these conditions, the uncertainties are similar to the absolute differences measured between fuels (typically ±2 cm/s) based on the data reported in the various sources. Bradley *et al.* [26] reported that laminar burning velocities for ethanol were much greater than *iso*-octane at 1 bar and 300–400 K. However, for 5 bar at 358 K, laminar burning velocities of 0.21–0.32 m/s were reported for ϕ=0.8–1.0. Those were very similar to the values for *iso*-octane reported for the same conditions in earlier work by Bradley and co-workers [23]; however, ethanol had greater temperature dependence than

hydrocarbons. For comparison, the correlations of [22] give at the same conditions ~0.17–0.27 m/s for *iso*-octane and ~0.22–0.30 m/s for indolene (standardised gasoline without additives), also suggesting marginally lower values than ethanol. The effect of cellularity on the Metghalchi and Keck [22] data has been addressed in the very recent work of Marshall *et al.* [34]. However, the differences between [34] and [22] were very small around stoichiometry for *iso*-octane at engine-like conditions, as can be seen in **Table 4**; nevertheless, the data of [34] confirm *iso*-octane's marginally lower laminar burning velocity at engine-like conditions than ethanol's (of the order 1 cm/s). Butanol laminar velocity data have only very recently become available [29–32, 43]; these have reported ~10% lower values than ethanol at atmospheric pressure but very similar or marginally higher values at higher pressures for the same temperatures. Specifically, Gu *et al.* [29, 43] reported values of laminar burning velocity between 0.45–0.5 m/s for similar temperatures to those at ignition timing of the current study.

Most of the existing data on laminar burning velocities have not accounted for residual gas fraction, especially with the alcohol fuels, hence the different sensitivity of such burning velocities to the residual fraction in the engine is not currently known and could potentially be a factor in explaining the differences observed in engines and combustion bombs. One of the oldest studies that considered the effect of residuals is that of Metghalchi and Keck [22] for *iso*-octane, indolene and methanol fuels; reductions by 35–45% were noted for residual gas fractions in the range 0.15–0.20, typical of SI engines at low load. The recent data of Marshall *et al.* [34] that addressed the effect of cellularity illustrated reductions reaching 50% for residual fractions of 0.2 for both *iso*-octane and ethanol fuels. Recent work with gasoline by Jerzembeck *et al.* [28] found laminar burning velocities for gasoline at 10 bar and 373 K between 0.12–0.22 m/s for equivalence ratios ϕ=0.7–1.0 which dropped to 0.05–0.1 m/s with a O_2 mole fraction in air of 0.15 (compared to 0.21 previously). The allowance for residual gas fraction in estimating burning velocities for combustion analysis in engines is therefore critical for accurate interpretation of results.

In order to make a basic comparison with the flame data of **Fig. 11**, a calculation was performed. Using the Metghalchi and Keck [22] correlation for the laminar velocity of *iso*-octane at ϕ=1.0 and with a residual gas fraction of 0.18, the laminar burning velocity at spark-timing conditions (~3 bar, 400 K) was calculated to be 0.24 m/s; the Marshall *et al.* [34] correlation yielded a value of 0.20 m/s. Using the ratio of unburned to burned densities for *iso*-octane at ignition timing, the initial burning velocity measured from the data of **Fig. 11** at 5° CA AIT, hence for flame radii smaller than 1 mm, was ~0.20 m/s, *i.e.* very close to those of [22, 34]. The velocities measured for all fuels from **Fig. 11** were very close and in agreement with the very small differences observed in **Table 4**. Higher spatial and temporal imaging resolution, focused solely on this very early stage of combustion, could allow more insights and detailed comparisons between fuels; nevertheless, it is still interesting that the basic trends are replicated even with a configuration aimed at studying the whole of the first 30° CA AIT.

Combustion Diagrams

The regimes of combustion for the different fuels used were identified on typical combustion diagrams. Whether the necessary resolution exists in terms of uncertainties in calculating the required parameters to make use of such diagrams a meaningful exercise of categorisation between the combustion regimes of different fuels, is a matter of continued debate due the numerous assumptions inherent in turbulent combustion models; clearly more experimental data are necessary from combustion bombs and optical

engines in order to resolve this matter fully. Nonetheless, they are the only tools currently available to classify different regimes of combustion, and so they are of value as long as they are interpreted in light of their inherent imperfections and known shortcomings.

The calculations for identifying the regimes of operation in those diagrams were based on turbulence intensity value of u'=2.25 m/s (as per PIV measurements [40]) and an integral length scale of 2 mm (as devised earlier). A constant u' was used for simplicity for all fuels, but based on earlier discussion on the effect of injection strategy on RMS velocity, difference of up to 10% could exist and this has been taken under consideration in the discussion below.

For analysis of the combustion process in the engine with respect to combustion diagrams, all relevant non-dimensional numbers, Damköhler (Da), Karlovitz (Ka), Reynolds (Re_L) and Lewis (Le), as well as the laminar flame thickness δ_l, were calculated. Values of specific heats, thermal conductivity, density and viscosity of the mixtures used expressions given in Poling *et al.* [64] or values from Yaws [65]. The binary diffusion coefficient for Le was based on both oxygen and the fuel as deficient reactants to produce 'lean' and 'rich' values, while the equivalent 'stoichiometric' value was based on the average of these two values, following the methodologies adopted by Bradley and co-workers [66–68]. Although the laminar burning velocity of the specific gasoline used in the current study was known, most of the transport properties were not known and the properties of *n*-Pentane were used instead for this exercise (*n*-Pentane is a representative light fraction of gasoline and it is the light fractions of gasoline that have been found to dictate primarily the spray formation and mixture preparation process across a range of conditions [44, 45]).

It is reiterated that the laminar burning velocity u_l for high pressure and temperature conditions for the different fuels in **Table 4** carry a typical uncertainty of ±0.02 m/s, hence in practice there is a great similarity in u_l amongst fuels for fixed ϕ=1.0, and it may be primarily the differences in ϕ and temperature/pressure that may lead to effects in laminar burning. Fixed values of ϕ, temperature and pressure were used for the calculation of the laminar burning velocities of all fuels on the combustion diagrams; this was a decision for wider applicability of the discussion; however, the differences in ϕ amongst fuels measured by FFID at the spark plug location, as well as the small differences in temperature and pressure, have been taken under consideration in the analysis below and comments are made where appropriate.

In the Abraham diagram [69] shown in **Fig. 21**, while three regions labelled A, B and C were highlighted to refer to calculations using different initial conditions, it is important to bear in mind that such fundamental analysis can only be made on an order of magnitude basis so that transitions between different regions in the diagrams should not be taken to indicate step changes in combustion characteristics. In region A, the conditions were 300 K, 1 bar. Region B was calculated at 400 K, 3 bar and referred to engine operation at around ignition timing. Region C was highlighted to indicate regions of the diagram that would be occupied if lower values of laminar burning velocity were used, for example to reflect the effects of combustion residuals or lean operation. For both regions A and B there was a clear trend towards methane being separated from the main group of liquid fuels. It was also clear that methane flames fell below the η/δ_l=1 line for condition A (where η is the Kolmogorov microscale), while the remainder of the fuels were either on the line or above it, corresponding to η/δ_l>1. This line also defined the boundary of the 'flame-sheet' or 'reaction-sheet' regime, where the smallest turbulent scales are larger than the laminar-flame thickness and the timescale of turbulent straining τ_η is large compared with the laminar-flame timescale τ_l, hence

combustion can occur in thin flame sheets. In the area where methane flames fell, η is smaller than δ_l, hence turbulent motions within the reaction sheet could disrupt the convective-diffusive balance in the preheat zone ($\tau_\eta < \tau_l$) and the straining could extinguish the flame.

The calculations showed that Da appeared to scale with fuel molecular weight, such that methane produced the lowest value and *iso*-octane the highest in both regions A and B. For all the fuels at ignition timing conditions the fuel trends remained the same, although the absolute values travelled diagonally along the $\eta/\delta_l=1$ boundary. The turbulent Reynolds numbers, Re_L, were also quite similar at ignition timing conditions, showing a maximum difference of ~15% between the lowest for methane and the largest for butanol. The two alcohols also had marginally higher Re_L compared to *iso*-octane and gasoline. It could be seen that in Region B, methane lay above the $\eta/\delta_L=1$ boundary of the 'flame-sheet' regime, with the alcohols also close to this boundary, and the other two hydrocarbons located well within the 'flame-sheet' regime. Considering uncertainties in the laminar burning velocities used (*e.g.* due to differences in local ϕ, temperature, residual, gas, *etc.*), higher values would produce higher Da and move the fuel groups vertically up in the diagram while lower values moved them downwards towards region C, *i.e.* below the transition line $\eta/\delta_L=1$.

The three operating conditions defined earlier by zones A, B and C were seen to be located around a transition boundary of the Peters diagram [70–71] in **(a)** of **Fig. 22**; particularly methane appeared to be always located inside the $Ka>1$ zone, with $Ka=2.6$ for condition B as shown in **Fig. 22**. This compared to values for *iso*-octane of $Ka=0.2$, whilst the other fuels produced values in-between these, with ethanol being very close to $Ka=1$. This was interesting in its own right because clear differences were observed in the visual appearance of methane flames versus those of *iso*-octane and gasoline, which these diagrams suggested might be due to flames falling within different combustion regimes. The dotted region C showed again how the fuels would relocate if lower laminar velocities were used in the calculations to reflect the higher residuals fraction, or differences in nominal ϕ and temperature/pressure; the differences between fuels were more likely to be accentuated under such conditions, as was indeed observed in the MFB data presented earlier for $\phi=0.83$. Peters in his modified diagram of [71] commented that a line at $Ka=100$ (close to the boundary area identified by the DNS work of Poinsot *et al.* [72] as a new limit of an extended flamelet regime) can be used to define a new 'thickened wrinkled flame' or thin reaction zones' regime above $Ka=1$; this corresponds to a length-scale of the order the flame's inner layer thickness that is about 10% of the laminar flame thickness. Even under $\phi=0.83$ and with residual gas fraction of the order 0.2, all points were well away from the upper boundary of this regime. For some mixtures to fall well within the core of this regime the Markstein number would most likely have to be negative, *e.g.* quite lean methane flames.

Diagram **(b)** of **Fig. 22** shows the Leeds combustion diagram [73]. In this diagram the effect of fuel type is represented by the Lewis number; Le governs the balance of thermal and mass diffusion across the flame front boundary and therefore describes the behaviour of the 'flame brush' as it affects the level of flame wrinkling via positive and negative stretch at the 'crests' and 'valleys' of the flame front. The correlations in **Fig. 22(b)** have been expressed in terms of the product KLe where K is the Karlovitz stretch factor calculated according to [26, 73]. At low values of KLe, a continuous wrinkled laminar flame sheet exists. As KLe increases, the flame becomes fragmented due to flame stretch until ultimately the flame can become totally quenched. The boundary of the extended flamelet regime suggested by Poinsot *et al.* [72] corresponds to $KLe=5.3$ on the Leeds diagram [73]. Calculations of the Karlovitz stretch factor at in-cylinder conditions

relevant to the timing of ignition used in the present study produced values of K~0.2. The symbols were plotted on the corresponding lines of constant KLe and at fully developed flames where $u'_k = u'$. Methane produced the lowest values of KLe~0.18 while *iso*-octane produced a KLe~0.345 with both the alcohols closer to methane values. Values for *iso*-octane increased to KLe~0.53 when Le values for lean conditions were used, while methane values remained ~0.18. This would suggest that the higher molecular weight fuels were generally more sensitive to flame stretch.

Markstein numbers (*Ma*) were considered from the studies of Lawes *et al.* [36] for *iso*-octane, methane and methanol, from Bradley *et al.* [26] for ethanol, from Sheppard and Lawes [60] for gasoline and from Gu *et al.* [29, 43] for butanol. The trends of the *Ma* with respect to ϕ show that methane has a near inverse relationship in comparison to all the other fuels; ethanol and butanol show similar trends to those of *iso*-octane and gasoline. Specifically, at atmospheric pressure and temperature, methane's *Ma* is always positive with values 2–7 for ϕ=0.7–1.2, whilst *iso*-octane's is always negative with a value of about 7 at ϕ=0.7 that is increasing to about 3 at ϕ=1.0, only to decrease again to levels of about 6 at ϕ=1.4 [75]. When temperature is increased to 358 K at 1 bar, methane's *Ma* remains positive with a value close to 3 at ϕ=0.8, increasing steadily to about 7 at ϕ=1.2. However, *iso*-octane's *Ma* switches over to positive values, starting from about 14 at ϕ=0.8 and decreasing steadily to zero levels at ϕ=1.3. For ethanol at 1 bar and 358 K, *Ma* is about 5–6 throughout ϕ=0.7–1.0, but it then reduces to levels of about 2 at ϕ=1.4. When pressure is increased to 5 bar, there is a double effect on combustion; higher pressure reduces Karlovitz factors and leads to a diminished stabilising effect of stretch on the flame, whilst simultaneously it also reduces *Ma* and leads to an inverted effect of the positive stretch, especially for lean mixtures. For methane at 5 bar and 358 K, *Ma* is about 1 at ϕ=0.7, increasing to about 2 at ϕ=1.0 and then to 6 at ϕ=1.3, whilst for *iso*-octane, *Ma* is about 8 at ϕ=0.8, decreasing to levels of about 1 at ϕ=1.2 [36]. For gasoline, *Ma* shows a much smaller dependence on equivalence ratio, as it has a value close to 6 at ϕ=0.8, decreasing to about 3 at ϕ=1.2 [60]. For ethanol, *Ma* is close to 6 at ϕ=0.7 but it then drops to zero levels at ϕ=1.3 and to a value of about 1 for ϕ=1.4 [26]; the trend is similar for butanol in terms of negative and positive values [29, 43].

All these values have been quoted to show that, primarily at the conditions in the engine close to stoichiometry, there is a trend of lower *Ma* for those fuels whose flames produced faster burning velocities in the engine (about 3, 4, 5.5 and 6 for methane, ethanol, gasoline and *iso*-octane, respectively). These results were therefore consistent with the assumption that moderate stretching could strengthen the localised burning velocity for Le<1 and suggested that methane flames in particular might be benefiting from this in the engine compared to the slower *iso*-octane and gasoline flames. Perhaps a modified combustion diagram that is a function of *Ma* can provide better interpretation of these data, especially in the context of engine flames and different fuels; there are probably sufficient data on *Ma* available now and the time is mature to generate new correlations.

SUMMARY AND CONCLUSIONS

The current paper presented results from a detailed optical study of combustion of gasoline, *iso*-octane, methane, ethanol and butanol fuels in a direct-injection spark-ignition engine. The liquid fuels were injected from a multi-hole injector located centrally in the combustion chamber in close proximity to the spark plug using 150 bar injection pressure. Methane was employed by injecting it into the inlet plenum of the engine to

provide a benchmark case for well-mixed 'homogeneous' mixture preparation. Various key operating conditions were examined, stoichiometric (ϕ=1) and lean (ϕ=0.83) mixtures, engine coolant temperatures (20 °C and 90°C). The engine speed was fixed to 1500 RPM with 0.5 bar intake pressure. The crank-angle resolved flame chemiluminescence images were post-processed to infer rates of flame growth and in-cylinder motion for all fuels averaged over 100 consecutive engine cycles for each test case. Laminar and turbulent burning velocity data were collected from the literature at engine relevant conditions to aid interpretation of the results. Analysis was further carried out with respect to combustion diagrams in order to provide a framework for comparison with current knowledge. The main conclusions of this study can be summarised as follows:

- Following ignition timing, flame growth for ϕ=1 was fastest for ethanol, followed by butanol, gasoline and *iso*-octane. Methane was slow during the very first 10° CA of combustion but it achieved values of flame growth speed of 10–13 m/s, similar to those of the alcohols, at 20–25°CA AIT. The trends amongst fuels were broadly similar at 20 °C and 90 °C, but the largest measured values of growth speed were about 5–10% higher at 90 °C.

- When the fuels were compared at fixed flame radii, methane had typically the fastest flame speed, but both alcohols achieved similar speeds to methane at a size of 15 mm in radius; the trend was clearer at 90 °C. Overall both alcohols exhibited very similar speeds with respect to flame radius, whilst *iso*-octane was always the slowest, ~25–30% slower at 15 mm flame radius than the other fuels; gasoline's behaviour was in-between that of alcohols and *iso*-octane.

- At ϕ=0.83, methane at 20 °C exhibited very similar MFB curve to that of ethanol, but at 90 °C it was clearly slower than ethanol, but of similar burning rate to that of butanol throughout the combustion process. Gasoline and *iso*-octane where both slower than all the other fuels. The timing of 10% MFB was retarded by about 5 °CA for all fuels in comparison to ϕ=1. The alcohols were generally more robust to changes in fuelling with respect to cyclic variability than the liquid hydrocarbons.

- Turbulent burning velocities were calculated from the engine flames of *iso*-octane, gasoline and methane at a size of 3 times the integral length scale and compared with data from combustion bomb experiments at carefully scaled conditions; the differences obtained between engine and bomb were ~5%, a very close match. For a size of 5–10 times the integral length scale, comparison with available ethanol data from the combustion bomb showed a difference of ~10%; this can be attributed to effects of in-cylinder large-scale bulk motion and anisotropy that cannot be easily scaled for. Butanol burning velocity was slower than ethanol's by about 8% but faster than gasoline's by about 5%, an interesting result when considering the absence of detailed turbulent burning velocity data for butanol from combustion bombs.

- A measure of flame stretch was calculated for all fuels on the basis of the calculated flame radii and growth speeds. At fixed flame radii stretch rates at 20 °C were initially highest for methane, then ethanol, butanol and *iso*-octane; gasoline showed very similar behaviour to *iso*-octane. At 90 °C, *iso*-octane and gasoline still showed very similar stretch rates, while ethanol separated from methane more clearly; butanol showed very similar stretch rates to the liquid hydrocarbons.

- All fuels showed an overall tendency for flame motion towards the exhaust valves which was explained by available PIV data. Methane showed very similar paths of motion at 20 °C and 90 °C. The liquid fuels

showed clear differences between 20 °C and 90 °C. At 20 °C the paths of motion of the two single-component fuels with the highest boiling points, *iso*-octane and particularly butanol, were biased towards the side of the combustion chamber where previous studies have shown significant fuel wall impingement. Interestingly, at 90 °C both alcohols followed very similar flame centroid paths to one another, whilst *iso*-octane and gasoline also exhibited similar behaviour to one another, all having behaviour more akin to methane's.

- The speed of flame centroid displacement from the spark-plug location during combustion was calculated in two forms to distinguish effects from large-scale bulk flow, 'global' displacement speed, and smaller scales, 'local' displacement speed. It was found that the 'global' speed was of the order 2 m/s and remained fairly stable throughout the combustion for all fuels; this value agreed well with PIV data in the same engine. The 'local' flame centroid speed exhibited peak values of ~3 m/s at 10–15° CA AIT (at flame size of 2–5 mm in radius), decreasing to values of ~1 m/s or lower at 25 °CA AIT (~15 mm flame radius), especially at 90 °C.

- The flames of both alcohols and those of methane showed noticeable differences in visual contrast or 'texture', and their average luminosities were lower than those of *iso*-octane and gasoline. These fuels produced a more opaque flame appearance, with less contrast within the flame, for which no single cause could be attributed on the basis of the current set of data (although various speculations could be made).

- Analysis of mixture transport properties for all fuels suggested that methane and the alcohols could fall within the transition region of the 'corrugated flame' to 'thin reaction zone' combustion regimes which has been associated with partially 'thickened' flame fronts. The calculated Lewis numbers of the fuels were also consistent with this analysis. There was also a trend of lower Markstein numbers for those fuels whose flames produced faster flame speeds in the engine and higher numbers for the slowest fuels.

Further work could focus on Laser-sheet flame tomography and OH LIF with high spatial resolution in order to establish whether the visual characteristics observed from natural light flame images can be related to fundamental differences in the flame front characteristics (*e.g.* see [76, 77] for similar work with hydrogen fuelling). Quantitative analysis of the degree of wrinkling and large-scale distortion of the flames (*e.g.* based on methods in [78]) will allow study of turbulence and Lewis number effects in greater detail and with a view of improving current combustion diagrams to reduce the order of magnitude limitations in the transitions between burning regimes, especially validated over many fuels in practical combustion systems; available data on Markstein numbers may also be useful for development of new combustion diagrams. Combustion spectroscopy will also add another layer of detail that could provide interpretation for the visual differences in the flame chemiluminescence images of the fuels, especially if in conjunction with studies of regulated and unregulated emissions (*e.g.* particulates and aldehydes).

REFERENCES

1. Kabasin, D.F., Hurter, T., Lamers, R., Hoyer, K. and Kazour, J., (2009), "Heated Injectors for Ethanol Cold Starts", SAE Paper 2009-01-0615.

2. Brinkman, N.D., (1981), "ethanol Fuel – A Single Cylinder Engine Study of Efficiency and Exhaust Emissions", SAE Paper 810345.

3. Gautam, M. and Martin D.W., (2000), "Combustion Characteristics of Higher Alcohol/Gasoline Blends", Proceeding of IMechE, Part A, Vol. 214, pp. 497–511.

4. Davis, G.W. and Heil, E.T., (2000), "The Development and Performance of a High Blend Ethanol Fueled Vehicle", SAE Paper 2000-01-1602.

5. Al-Farayedhi, Al-Dawood, A.M. and Gandhidasan, P., (2004), "Experimental Investigation of SI Engine Performance Using Oxygenated Fuel", Transactions of ASME, Journal of Engineering Gas Turbines and Power, Vol. 126, pp 178–191.

6. Nakata, K., Utsumi, S., Ota, A., Kawatake, K., Kawai, T. and Tsunooka, T., (2006), "The Effect of Ethanol on a Spark Ignition Engine", SAE Paper 2006-01-3380.

7. Topgül, T., Yücesu, H.S., Cinar, C. and Koca, A., (2006), "The Effects of Ethanol-Unleaded Gasoline Blends and Ignition Timing on Engine Performance and Exhaust Emissions", Renewable Energy, Vol. 31, pp. 2534–2542.

8. Guerrieri, D.A., Caffrey, P.J. and Rao, V., (1995), "Investigation into the Vehicle Exhaust Emissions of High Percentage ethanol Blends", SAE Paper 950777.

9. Gautam, M., Martin, D.W. and Carder, D., (2000), "Emissions Characteristics of Higher Alcohol/gasoline Blends", Proceedings of IMechE, Part A, Vol. 214, pp. 165–182.

10. Sandiquist H., Karlsson, M. and Denbratt, I., (2001), "Influence of ethanol Content in Gasoline on Speciated Emissions from a Direct-Injection Stratified Charge SI Engine", SAE Paper 2001-01-1206.

11. Martinez, F.A. and Ganji, A.R., (2006), "Performance and Exhaust Emissions of a Single-Cylinder Utility Engine Using Ethanol Fuel", SAE Paper 2006-32-0078.

12. Zhu, G., Stuecken, T., Schock, H., Yang, X., Hung, D. and Fedewa, A., (2008), "Combustion Characteristics of a Single-Cylinder Engine Equipped with Gasoline and Ethanol Dual-Fuel Systems", SAE Paper 2008-01-1767.

13. Aleiferis, P.G., Malcolm, J.S., Todd, A.R., Cairns, A. and Hoffmann, H., (2008), "An Optical Study of Spray Development and Combustion of Ethanol, *iso*-Octane and Gasoline Blends in a DISI Engine", SAE Paper 2008-01-0073.

14. Aleiferis, P.G., Serras-Pereira, J., van Romunde, Z., Caine, J. and Wirth, M., 2010, "Mechanisms of Spray Formation and Combustion from a Multi-Hole Injector with E85 and Gasoline", Combustion and Flame, Vol. 157, pp. 735–756

15. Szwaja, S., Naber, J.D., (2010), "Combustion of *n*-Butanol in a Spark-Ignition Engine", 17th International Symposium on Alcohol Fuels, Fuel, Vol. 89, pp. 1331–1748.

16. Malcolm, J.S., Aleiferis, P.G., Todd, A.R. and Cairns, A., Hume, A., Blaxill, H., Hoffmann, H. and Rueckauf, J., (2007), "A. Study of Blended Alcohol Fuels in a New Optical Spark-Ignition Engine", International Conference on Internal Combustion Engines: Performance, Fuel Economy and Emissions, December 2007, IMechE, London, UK, pp. 223-234.

17. Todd, A., Fraser N, Aleiferis, P.G., Malcolm J. and Cairns, A., 2010, "A Study of Alcohol Blended Fuels in an Unthrottled Single-Cylinder Spark-Ignition Engine", SAE World Congress, Detroit, USA, SAE Paper 2010-01-0618.

18. Wallner, T., Miers, S.A. and Mconnell, S., (2009), "A Comparison of Ethanol and Butanol as Oxygenates Using a Direct-Injection, Spark-Ignition Engine", Transactions of ASME, Journal of Engineering for Gas Turbine and Power, Vol. 131, pp. 032802-1–032802-9.

19. Smith, J.D. and Sick, V., (2007), "The Prospects of Using Alcohol-Based Fuels in Stratified-Charge Spark-Ignition Engines", SAE Paper 2007-01-4034.

20. Gülder, Ö.L., (1984), "Burning Velocities of Ethanol–*iso*-Octane Blends", Combustion and Flame, Vol. 56, pp. 261–168, 1984.

21. Gülder, O.L., (1984), "Correlations of Laminar Combustion Data for Alternative SI Engine Fuels", SAE Paper 841000.

22. Metghalchi, M. and Keck, J.C., (1982), "Burning Velocities of Mixtures of Air with Methanol, *iso*-Octane and Indolene at High Pressure and Temperature", Combustion and Flame, Vol. 48, pp. 191–210.

23. Bradley, D., Hicks, M., Lawes, M., Sheppard, C.G.W. and Woolley, R., (1998), "The Measurement of Laminar Burning Velocities and Markstein Numbers for *iso*-Octane–Air and *iso*-Octane–*n*-Heptane–Air Mixtures at Elevated Temperatures and Pressures in an Explosion Bomb", Combustion and Flame, Vol. 115 pp. 126–144.

24. Gu, X.J., Haq, M.Z., Lawes, M. and Wooley, R., (2000), "Laminar Burning Velocity and Markstein Lengths of methane-Air Mixtures", Combustion and Flame, Vol.121, pp. 41–58.

25. Liao, S.Y., Jiang, D.M., Huang, Z.H., Zeng, K. and Cheng, Q., (2007), "Determination of Laminar Burning Velocities for Mixtures of Ethanol and Air at Elevated Temperatures", Applied Thermal Engineering, Vol. 27, pp. 374–380.

26. Bradley, D., Lawes, M. and Mansour, M.S., (2009), "Explosion Bomb Measurements of Ethanol-Air Laminar Gaseous Flame Characteristics at Pressures up to 1.4 MPa", Combustion and Flame, Vol. 156, pp. 1462–1470.

27. Al-Shahrany, A.S., Bradley, D., Lawes, M. and Woolley, R., (2005), "Measurement of Unstable Burning Velocities of *iso*-Octane-Air Mixtures at High Pressure and the Derivation of Laminar Burning Velocities", Proceedings of the Combustion Institute, Vol. 30, pp. 225–232.

28. Jerzembeck, S., Peters, N., Pepiot-Desjardins, P. and Pitsch, H., (2009), "Laminar Burning Velocities at High Pressure for Primary Reference Fuels and Gasoline: Experimental and Numerical Investigation", Combustion and Flame, Vol. 156, pp. 292–301.

29. Gu, X., Huang, Z., Li, Q. and Chenglong, T., (2009), "Measurements of Laminar Burning Velocities and Markestein Lengths of *n*-Butanol-air Premixed Mixtures at Elevated Temperatures and Pressures", Energy and Fuels, Vol. 23, pp. 4900–4907.

30. Sarathy, S.M., Thomson, M.J., Togbe, C., Dagaut, P., Halter, F. and Mounaim-Rousselle, C., (2009), "An Experimental and Kinetic Modeling Study of *n*-butanol Combustion", Combustion and Flame, Vol. 156, pp. 852–864.

31. Beeckmann, J., Kruse, S. and Peters, N., (2010), ''Effect of Ethanol and *n*-Butanol on Standard Gasoline Regarding Laminar Burning Velocities'', SAE Paper 2010-01-1452.

32. Beeckmann, J., Rohl, O. and Peters, N., (2009), ''Numerical and Experimental Investigation of Laminar Burning Velocities of *iso*-Octane, Ethanol and *n*-Butanol'', SAE Paper 2009-01-2784.

33. Farrell, J.T., Johnston, R.J. and Androulakis, I.P., (2004), "Molecular Structure Effects on Laminar Burning Velocities at Elevated Temperature and Pressure", SAE Paper 2004-01-2936.

34. Marshall, S.P., Taylor, S., Stone, C.R., Davies, T.J. and Cracknell, R.F., (2011), "Laminar Burning Velocity Measurements of Liquid Fuels at Elevated Pressures and Temperatures with Combustion Residuals", Combustion and Flame, Vol. 158, pp. 1920–1932.

35. Vancoillie, J., Verhelst, S. and Demuynck, J., (2011), "Laminar Burning Velocity Correlations for Methanol-Air and Ethanol-Air Mixtures Valid at SI Engine Conditions", SAE Paper 2011-01-0846

36. Lawes, M., Ormsby, M.P., Sheppard, C.G.W. and Woolley, R., (2005), "Variation of Turbulent Burning Rate of Methane, Methanol, and *iso*-Octane Air Mixtures with Equivalence Ratio at Elevated Pressure", Combustion Science and Technology, Vol. 177, pp. 1273–1289.

37. Bradley, D., Lawes, M. and Mansour, M.S., (2011), "Correlation of Turbulent Burning Velocities of Ethanol-Air, Measured in a Fan-Stirred Bomb up to 1.2 MPa", Combustion and Flame, Vol. 158, pp. 123–138.

38. Serras-Pereira, J., Aleiferis, P.G., Richardson, D. and Wallace, S., "Characteristics of Ethanol, Butanol, *iso*-Octane and Gasoline Sprays and Combustion from a Multi-Hole Injector in a DISI Engine", SAE International Journal of Fuels and Lubricants, Vol. 1, pp. 893–909, SAE Paper 2008-01-1591, 2008.

39. Aleiferis, P.G., Serras-Pereira, J. and Richardson, D., 2011, "Imaging and Heat Flux Measurements of Impinging Sprays of Liquid Hydrocarbons and Alcohols in a Motoring and Firing Direct-Injection Spark-Ignition Engine", Fuel, Vol. 91, pp. 264–297.

40. Rimmer, J.E.T., Long, E.J., Garner, C.P., Hargrave, G.K., Richardson, D., Wallace, S., (2009), "The Influence of Single and Multiple Injection Strategies on In-Cylinder Flow and Combustion within a DISI engine", SAE Paper 2009-01-0660.

41. Williams, B., Ewart, P., Stone, R., Ma, H., Walmsley, H., Cracknell, R., Stevens, R., Richardson, D., Qiao, J. and Wallace, S., (2008), Multi-Component Quantitative PLIF: Robust Engineering Measurements of Cyclic Variation in a Firing Spray-Guided gasoline Direct Injection Engine", SAE Paper 2008-01-0469.

42. Serras-Pereira, J., Aleiferis, P.G., Richardson, D. and Wallace, S., 2007, "Mixture Formation and Combustion Variability in a Spray-Guided DISI Engine", Transactions of SAE, Journal of Engines, Vol. 116, No 3, pp. 1332-1356, Paper 2007-01-4033.

43. Gu, X., Huang, Z., Wu, S. and Li, Q., (2010), "Laminar Burning Velocities and Flame Instabilities of Butanol Isomer-Air Mixtures", Combustion and Flame, Vol. 157, pp. 2318–2325.

44. van Romunde, Z., Aleiferis, P.G., Cracknell, R.F. and Walmsley, H.L., (2007), "Effect of Fuel Properties on Spray Development from a Multi-Hole DISI Engine Injector", SAE Transactions, Journal of Engines, Vol. 116, No. 3, pp. 1313–1331, SAE Paper 2007-01-4032.

45. Aleiferis, P.G., Serras-Pereira, J., Augoye, A., Davies, T.J., Cracknell, R.F. and Richardson, D., 2010, "Effect of Fuel Temperature on In-Nozzle Cavitation and Spray Formation of Liquid Hydrocarbons and Alcohols from a Real-Size Optical Injector for Direct-Injection Spark-Ignition Engines", International Journal of Heat and Mass Transfer, Vol. 53, pp. 4588–4606.

46. Serras-Pereira, J., "Spray Formation and Combustion of Alcohols and Gasoline in a Direct-Injection Spark-Ignition Engine", PhD Thesis, University of London, 2010.

47. Ball, J. K., Raine, R. R. and Stone, C. R., (1998), "Combustion Analysis and Cycle-by-Cycle Variations in Spark Ignition Engine Combustion – Part 1: An Evaluation of Combustion Analysis Routines by Reference to Model Data", Proceedings of IMechE, Part D, Vol. 212, pp. 381–399.

48. Stone, C. R. and Green-Armytage, D. I., (1987), "Comparison of Methods for the Calculation of Mass Fraction Burned from Engine Pressure-Time Diagrams", Proceedings of IMechE, Part D, Vol. 201, No. 1, pp. 61–67.

49. Brunt, M. F. and Emtage, A. L., (1996), "Evaluation of IMEP Routines and Analysis Errors", SAE Paper 960609.

50. Cheng, W.K., Summers, T. and Collings, N., (1998), 'The Fast-Response Flame Ionisation Detector', Progress in Energy and Combustion Science, Vol. 24, pp. 89–124.

51. Price, P., Twiney, B., Stone, R., Kar, K. and Walmsley, H., (2007), "Particulate and Hydrocarbon Emissions from a Spray Guided Direct Injection Spark Ignition Engine with Oxygenate Fuel Blends", SAE Paper 2007-01-0472.

52. Dec, J.E., Davisson, M.L., Sjöberg, M., Leif, R.N. and Hwang, W., 2008, "Detailed HCCI Exhaust Speciation and the Sources of Hydrocarbon and Oxygenated Hydrocarbon Emissions", SAE Paper 2008-01-0053.

53. Wallner, T. and Frazee, R., 2010, "Study of Regulated and Non-Regulated Emissions from Combustion of gasoline, Alcohol Fuels and their Blends in a DI-SI Engine", SAE Paper 2010-01-1571.

54. Wallner, T., (2011), "Correlation between Speciated Hydrocarbon Emissions and Flame Ionization Detector Response for Gasoline/Alcohol Blends", Transactions of ASME, Journal of Engineering for Gas Turbines and Power, Vol. 133, pp. 082801-1– 082801-8.

55. Lotus Engine Simulation Software, http://www.lesoft.co.uk/index.html, 2010.

56. Beyrau, F., Weikl, M.C., Schmitz, I., Seeger, T. and Leipertz, A., (2006), "Locally Resolved Investigation of the Vaporization of GDI Sprays Applying Different Laser Techniques", Atomization and Sprays, Vol. 16, pp. 319–330.

57. Morley, C., (2005), "GASEQ: A Chemical Equilibrium Program for Windows", www.gaseq.co.uk.

58. Fraser, R.A. and Bracco, F.V., (1988), "Cycle-resolved LDV integral length scale measurements in an IC engine", SAE Paper 880381.

59. Beretta, G.P., Rashidi, M. and Keck, J.C., (1983), "Turbulent Flame Propagation and Combustion in Spark-Ignition Engines", Combustion and Flame, Vol. 52, pp. 217–245.

60. Sheppard, C.G.W. and Lawes, M., (2010), Personal Communication.

61. Lawes, M. and Saat, A., (2011), "Burning Rates of Turbulent *iso*-Octane Aerosol Mixtures in Spherical Flame Explosions", Proceedings of the Combustion Institute, Vol. 33, pp. 2047–2054.

62. Egolfopoulos, F.N., Du, D.X. and Law, C.K., (1992), "A Study on Ethanol Oxidation Kinetics in Laminar Premixed Flames", Flow Reactors, and Shock Tubes", 24th Symposium (International) on Combustion, pp. 833–841.

63. Malcolm, J.S., Behringer, M., Aleiferis, P.G., Mitcalff, J. and OudeNijeweme, D., 2011, "Characterisation of Flow Structures in a Direct-Injection Spark-Ignition Engine using PIV, LDV and CFD", SAE Paper 2011-01-1290.

64. Poling, B.E., Prausnitz, J.M. and O'Connell, J.P., (2001), "The Properties of Gases and Liquids", 5th Edition, McGraw Hill.

65. Yaws, C.L., (2003), "Yaws' Handbook of Thermodynamic and Physical Properties of Chemical Compounds", Knovel Electronic Database.

66. Abdel-Gayed, R.G., Bradley, D., Hamid, M.N. and Lawes, M., (1984), "Lewis Number Effects on Turbulent Burning Velocity", 20th Symposium (International) on Combustion, pp. 505–512.

67. Abdel-Gayed, R.G., Al-Khishali, K.J. and Bradley, D., (1984), "Turbulent Burning Velocities and Flame Straining in Explosions", Proceedings of the Royal Society of London, A 391, pp. 393–414.

68. Bradley, D., Haq, M.Z., Hicks, R.A., Kitagawa, T., Lawes, M., Sheppard, C.G.W. and Woolley, R., (2003), "Turbulent Burning Velocity, Burned Gas Distribution, and Associated Flame Surface Definition", Combustion and Flame, Vol. 133, pp. 415–430.

69. Abraham, J., Williams, F. A. and Bracco, F. V., (1985), "A Discussion of Turbulent Flame Structure in Premixed Charges", SAE Paper 850345.

70. Peters, N., (1986), "Laminar Flamelet Concepts in Turbulent Combustion", 21st Symposium (International) on Combustion, pp. 1231–1250.

71. Peters, N., (1999), "The Turbulent Burning Velocity for Large-Scale and Small-Scale Turbulence", Journal of Fluid Mechanics, Vol. 384, pp. 107–132.

72. Poinsot, T., Veynante, D., Candel, S., (1990), "Diagrams of Premixed Turbulent Combustion Based on Direct Simulation", 23rd Symposium (International) on Combustion, pp. 613–619.

73. Bradley, D., (1992), "How Fast Can We Burn?", 24th Symposium (International) on Combustion, pp. 247–262.

74. Bradley, D., Lawes, M. and Sheppard, C.G.W., (2000), "Combustion and the Thermodynamic Performance of SI Engines", Proceedings of IMechE, Part C, Vol. 214, pp. 257–268.

75. Bradley, (2009), "Combustion and the Design of Future Engine Fuels", Proceedings of IMechE, Part C, Vol. 223, pp. 2751–2765.

76. Aleiferis, P.G. and Rosati, M.F., 2012, "Flame Chemiluminescence and OH LIF Measurements in a Hydrogen-Fuelled Spark-Ignition Engine", International Journal of Hydrogen Energy, Vol. 37, pp. 1797–1812.

77. Aleiferis, P.G. and Rosati, M.F., 2012, Controlled Autoignition of Hydrogen in a Direct-Injection Optical Engine", Combustion and Flame, Vol. 159, pp. 2500–2515.

78. Aleiferis, P.G., Taylor, A.M.K.P., Ishii, K. and Urata, Y., 2004, "The Nature of Early Flame Development in a Lean-Burn Stratified-Charge Spark-Ignition Engine", Combustion and Flame, Vol. 136, pp. 283-302.

LIST OF TABLES

LIST OF FIGURES

Table 1. Optical Engine Specifications.

Engine Base Type	Prototype Head
Cycle	4-Stroke
Cylinders	1
Valves	2 Intake, 2 Exhaust
Bore	89.0 mm
Stroke	90.3 mm
Compression Ratio	11.15:1
Valve Timings	IVO 24°, IVC 274°, EVO 476°, EVC 6° CA ATDC

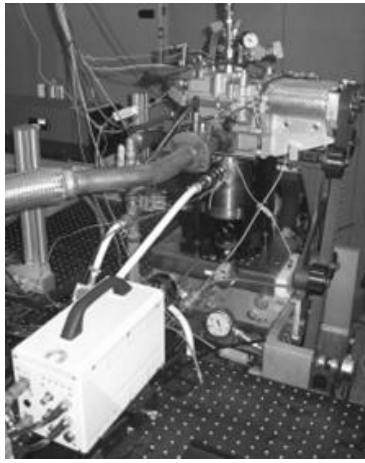**Table 2.** Fuel Injection Pulsewidths Used for all Fuels and Injection Strategies.

Fuel	Injection Pulse Durations [ms]	
	ϕ=1.0	ϕ=0.83
iso-Octane	0.90	0.74
Gasoline	0.90	0.74
Ethanol	1.38	1.14
Butanol	1.10–1.16	0.91–0.96
Methane	3.90	3.10

Table 3. Equivalence Ratio at the Spark Plug at Ignition Timing Measured by FFID.

Fuel	Equivalence Ratio, ϕ (Engine Temperature 90 °C)
iso-Octane	0.97
Gasoline	0.94
Ethanol	1.04
Butanol	0.99
Methane	1.00

Table 4. Laminar Burning Velocities from Various Sources at Conditions of Interest in SI Engines.

Source	T [K]	P [bar]	ϕ	Laminar Burning Velocity [cm/s]				
				Methane	Ethanol	Butanol	*iso*-Octane	Gasoline
Gu *et al.* [24]	300	1	1.0	36				
			0.8	26				
	358	1	1.0	48				
		5	1.0	26				
		10	1.0	20				
		1	0.8	38				
		5	0.8	17				
		10	0.8	12				
	428	5	1.0	35				
			0.8	24				
	400	3	1.0	38				
			0.8	27				
	450	3	1.0	46				
			0.8	35				
	450	5	1.0	40				
			0.8	27				
Bradley *et al.* [23]	358	1	1.0				47	
			0.8				40	
Jerzembeck *et al.* [28]	358	5	1.0				30	
		10	1.0				26	
		5	0.8				23	
		10	0.8				17	
	373	10	1.0				29	28
		10	0.8				17	17
Metghalchi and Keck [22] *iso*-Octane (1st column), Gasoline Marshall *et al.* [34] *iso*-Octane (2nd column), Ethanol	300	1	1.0		28		31, 29	33
			0.8		16		22, 23	20
	358	5	1.0		27		29, 29	31
			0.8		16		19, 22	21
	428	5	1.0		41		42, 41	45
			0.8		26		29, 31	32
	400	3	1.0		41		40, 40	42
			0.8		25		27, 31	31
	450	3	1.0		53		51, 50	54
			0.8		34		36, 38	40
	450	5	1.0		46		47, 45	50
			0.8		30		32, 34	36
Sheppard and Lawes [60]	358	5	1.0					31
			0.8					22
Farrell *et al.* [33]	450	3	1.0	60	61		56	
			0.8	44	54		47	
Gülder [21]	350	1	1.0		58		56	
			0.8		36		45	
Bradley *et al.* [26]	300	1	1.0		38			
			0.8		27			
	358	1	1.0		52			
		5	1.0		31			
		10	1.0		25			
		1	0.8		38			
		5	0.8		22			
		10	0.8		17			
	428	5	1.0		43			
	400	3	1.0		44			
	450	3	1.0		54			
	450	5	1.0		46			
Gu *et al.* [29]	413	2.5	1.0			41		
			0.8			23		
	443	1	1.0			46		
			0.8			36		
	443	2.5	1.0			40		
			0.8			26		
	473	2.5	1.0			49		
			0.8			29		
Gu *et al.* [43]	428	1	1.0			61		
			0.8			52		
	428	5	1.0			44		
Sarathy *et al.* [30]	350	0.9	1.0			44		
			0.8			29		
Beeckmann *et al.* [31, 32]	373	10	1.0		28	28	25	28
		10	0.8		18	18	17	21

Engine on Test Bed   Camera View

Fig. 1. Configuration of Single-Cylinder Optical Research Engine.
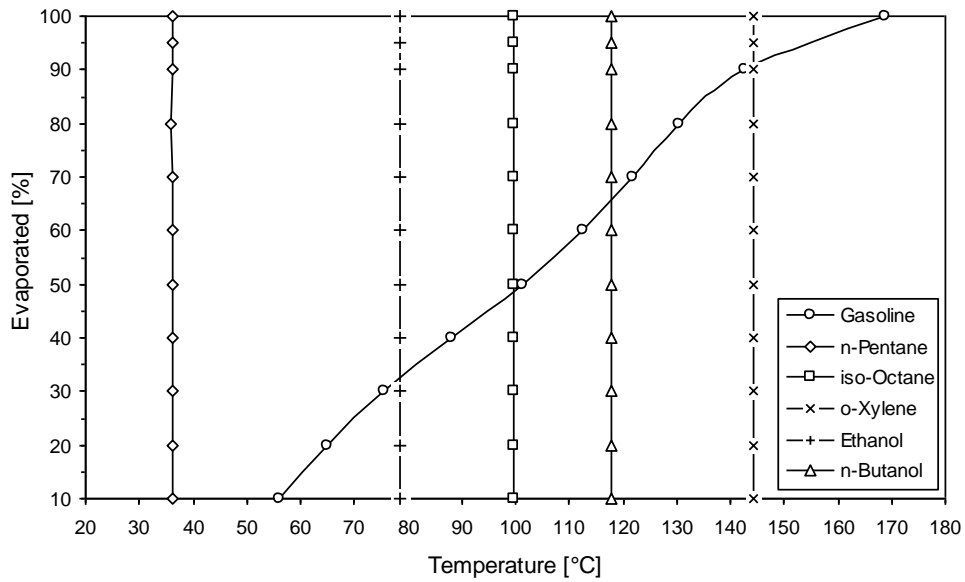
Fig. 2. Distillation Curve of gasoline and Boiling Points of Single-Component Fuels.
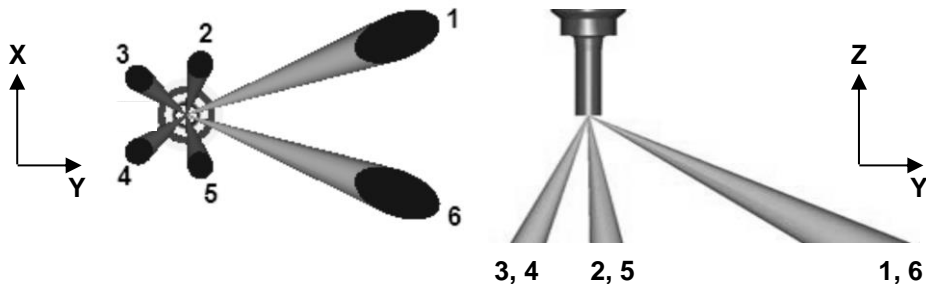
Fig. 3. Schematic of Injector and Spray Plumes.
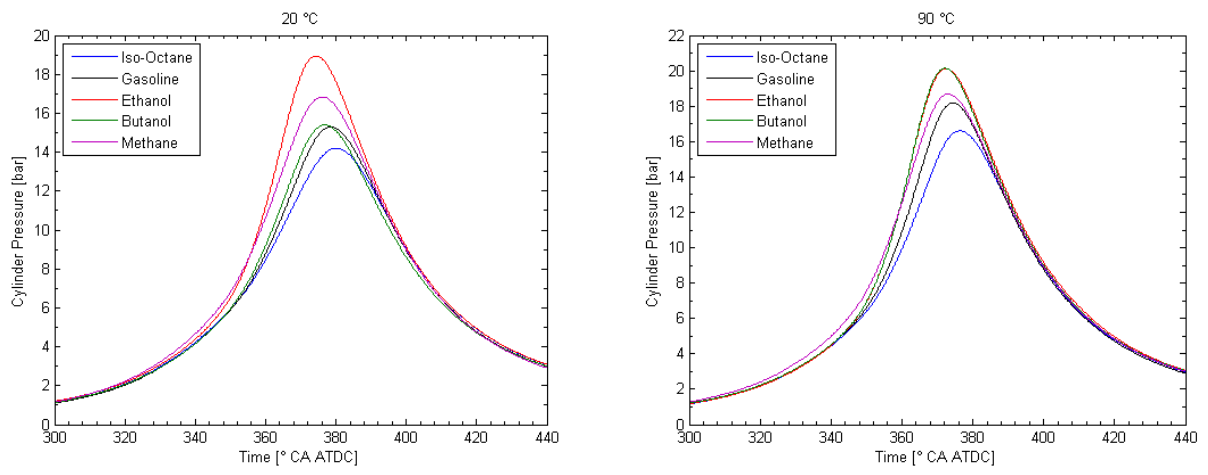
Fig. 4. In-Cylinder Pressure; ϕ=1.0, 20 °C and 90 °C.
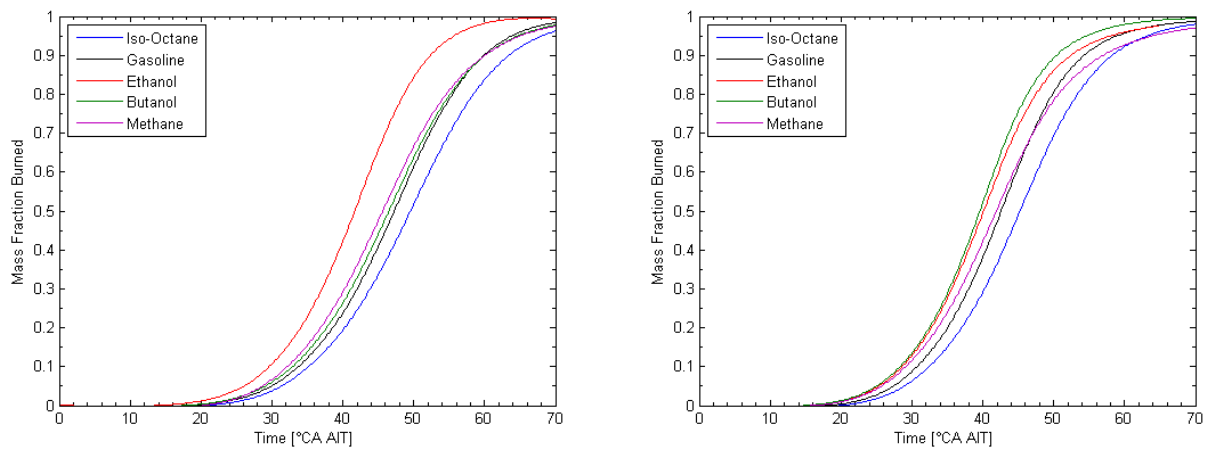
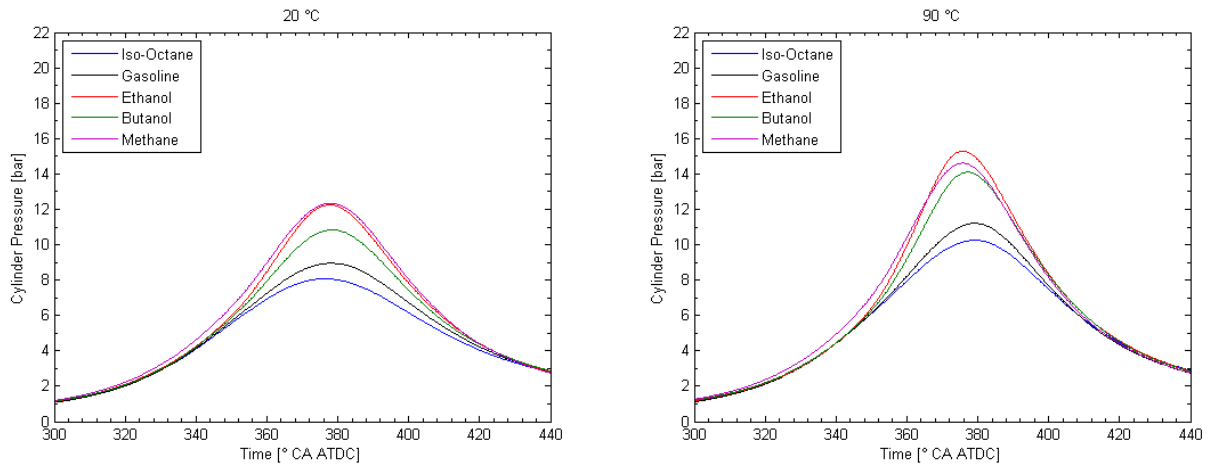**Fig. 5.** Mass Fraction Burned; ϕ=1.0, 20 °C and 90 °C.

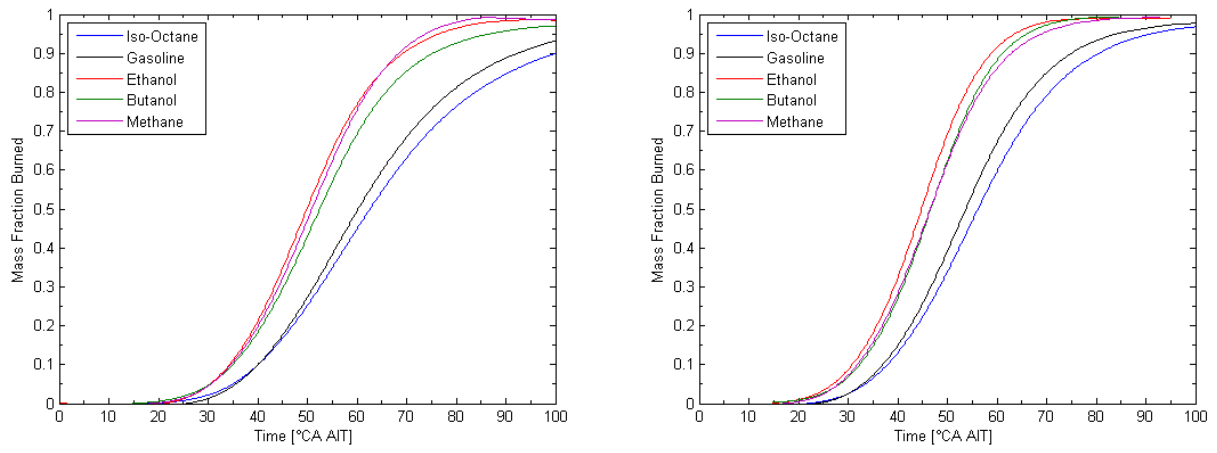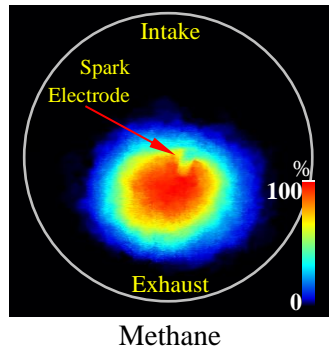**Fig. 6.** In-Cylinder Pressure; ϕ=0.83, 20 °C and 90 °C.

Fig. 7. Mass Fraction Burned; ϕ=0.83, 20 °C and 90 °C.
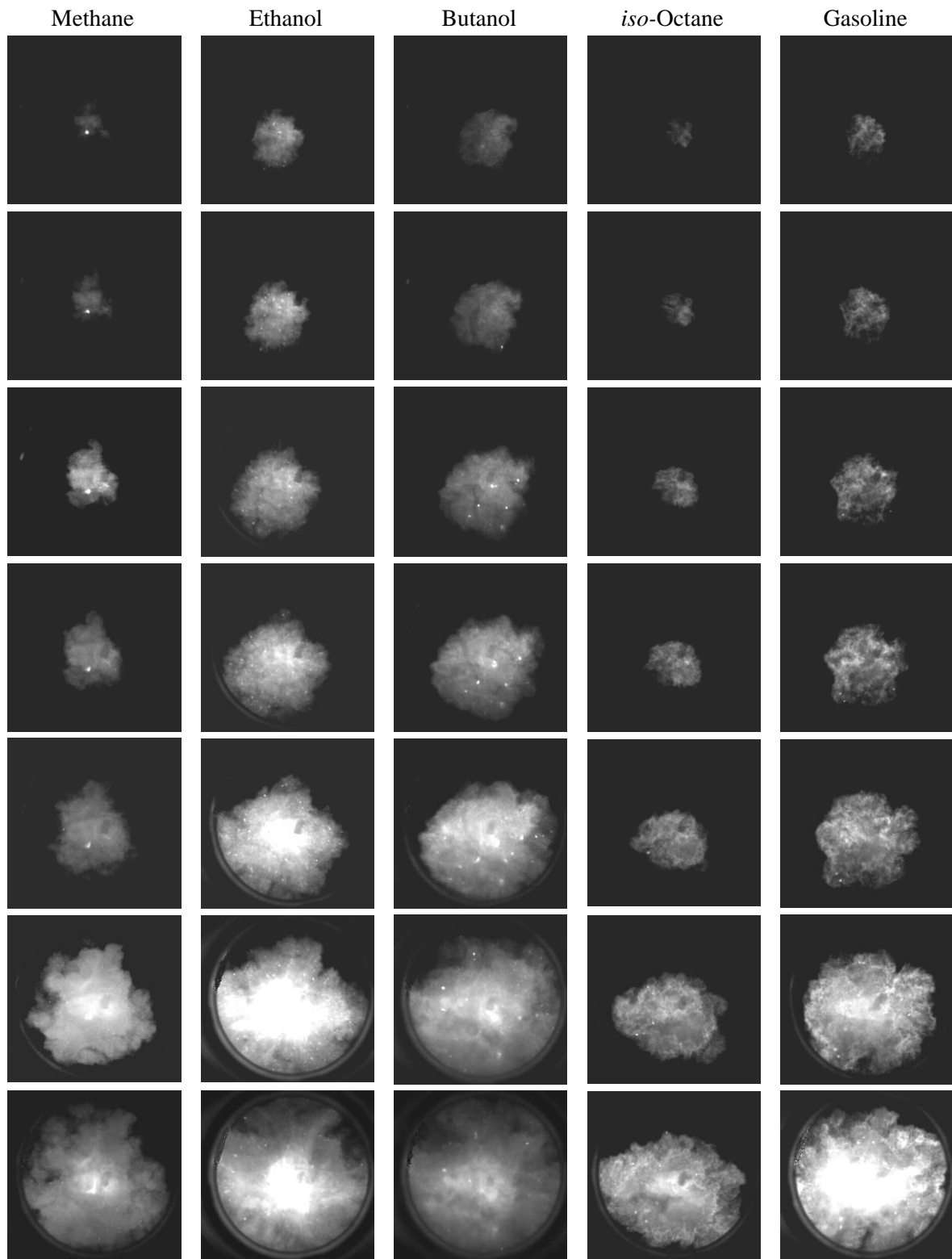
Fig. 8. Flame Development at 20°, 22°, 25°, 27°, 30°, 35° and 40° CA AIT (ϕ=1.0, 20 °C).
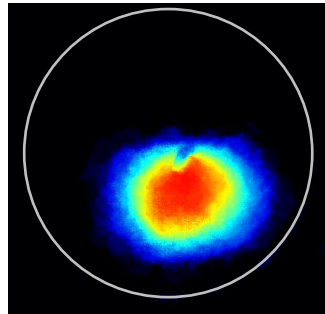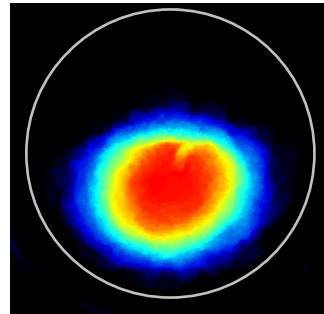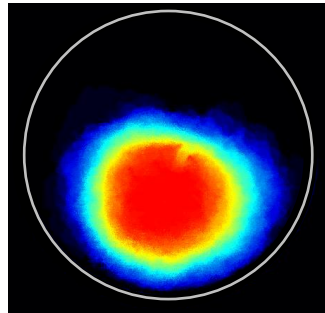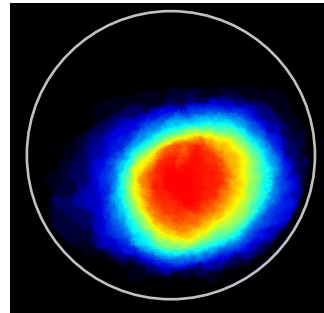
Fig. 9. Probability of Flame Presence at 25° CA AIT (ϕ=1.0, 20 °C).
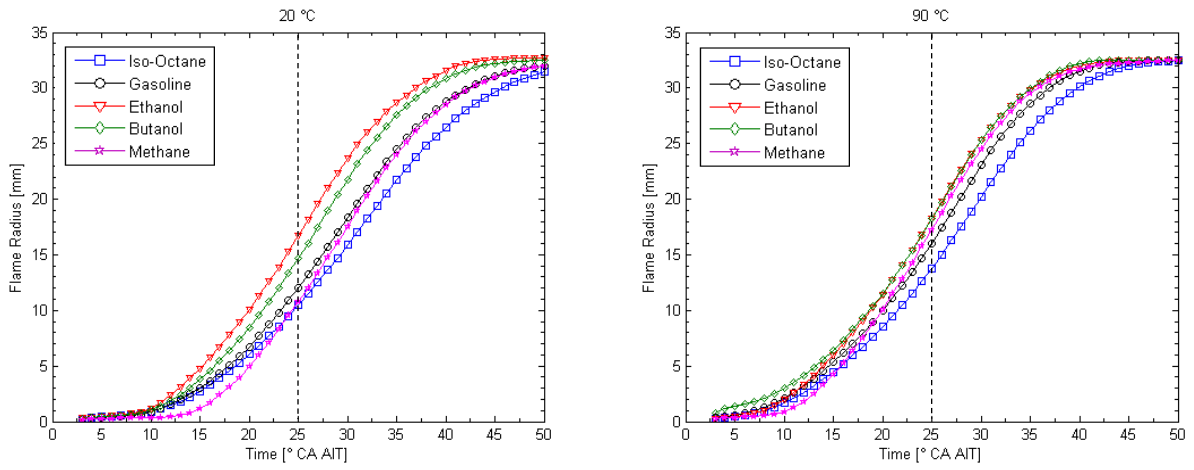
Fig. 10. Flame Radius; ϕ=1.0, 20 °C and 90 °C.
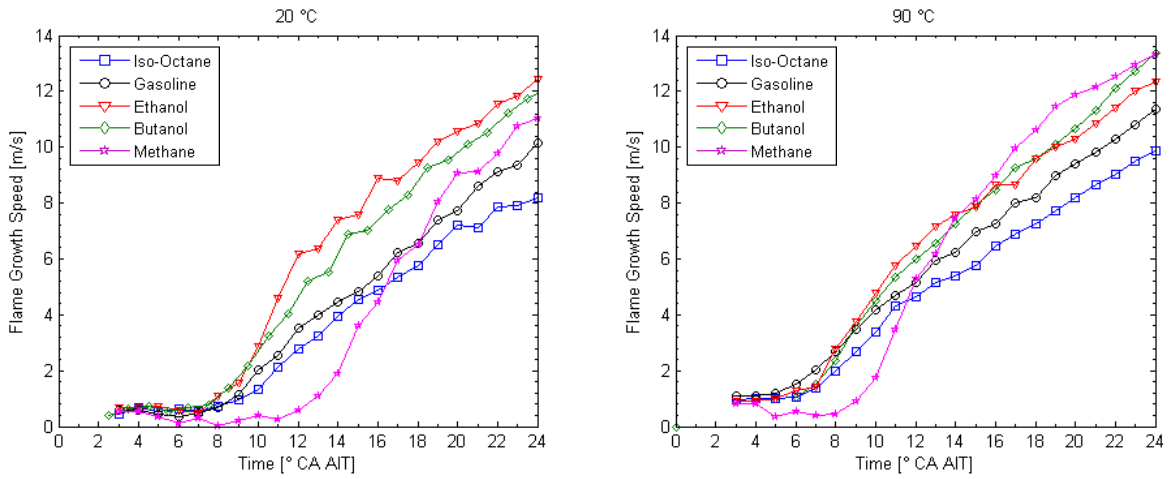
Fig. 11. Flame Growth Speed; ϕ=1.0, 20 °C and 90 °C.
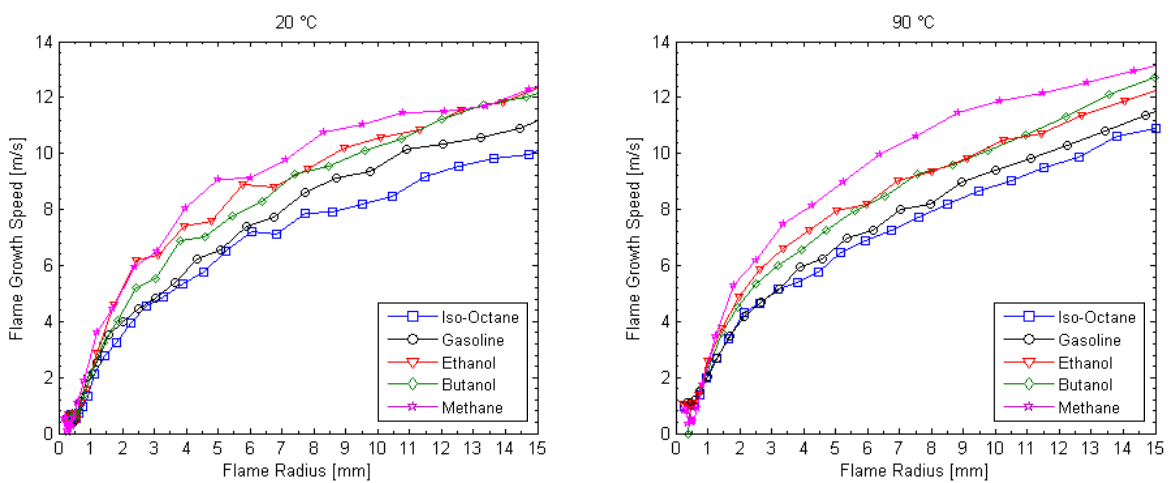
Fig. 12. Flame Growth Speed as a Function of Flame Radius; ϕ=1.0, 20 °C and 90 °C.
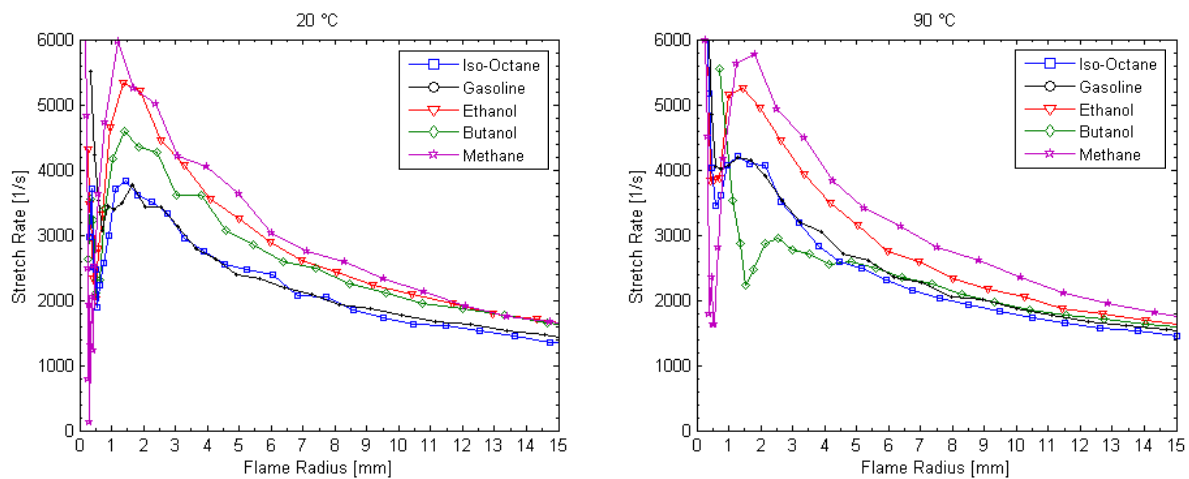
Fig. 13. Flame Stretch; ϕ=1.0, 20 °C and 90 °C.
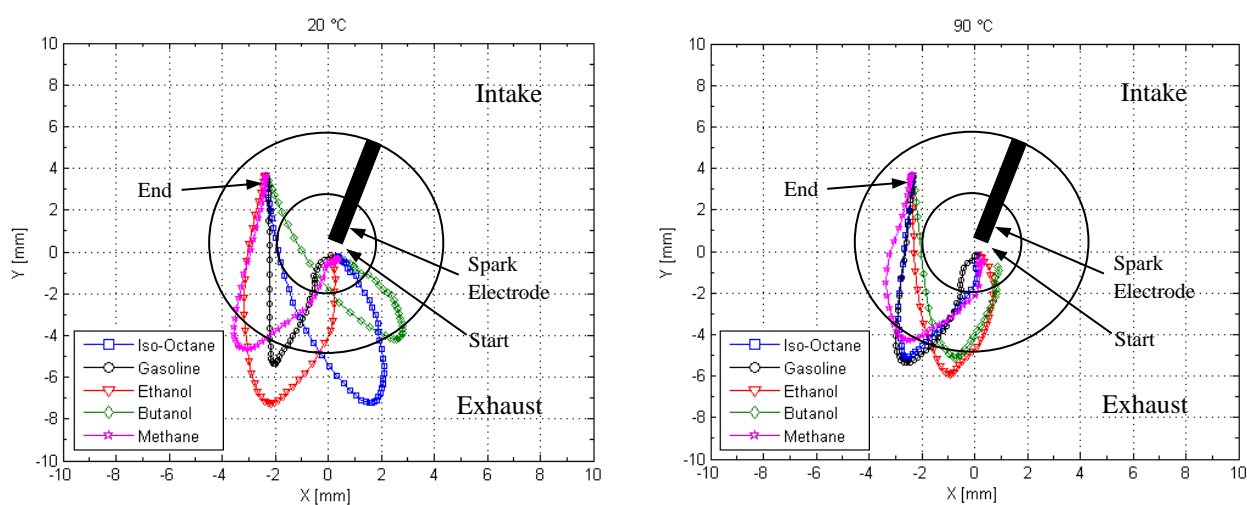
Fig. 14. Flame Centroid Paths; ϕ=1.0, 20 °C and 90 °C.
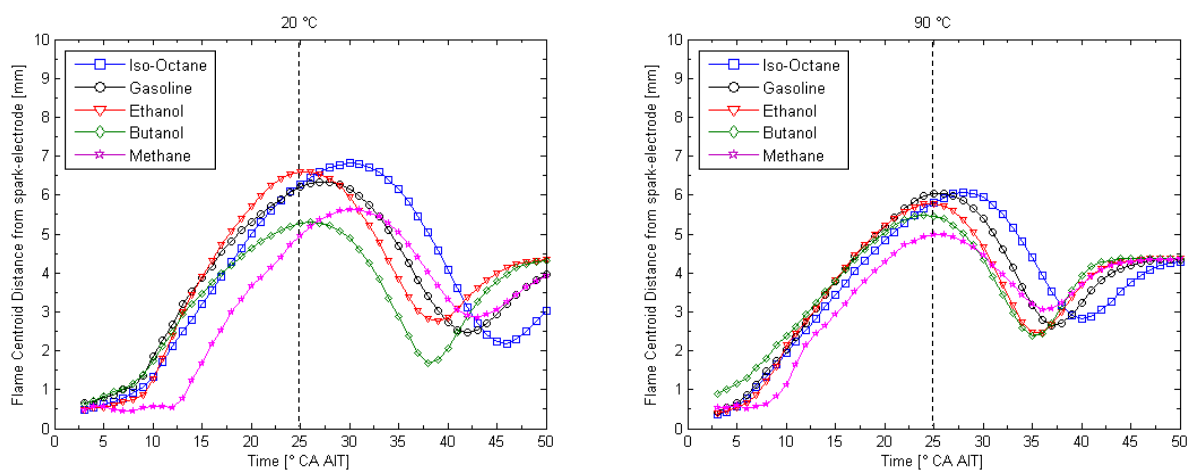
Fig. 15. Flame Centroid Distance from Spark Plug; ϕ=1.0, 20 °C and 90 °C.
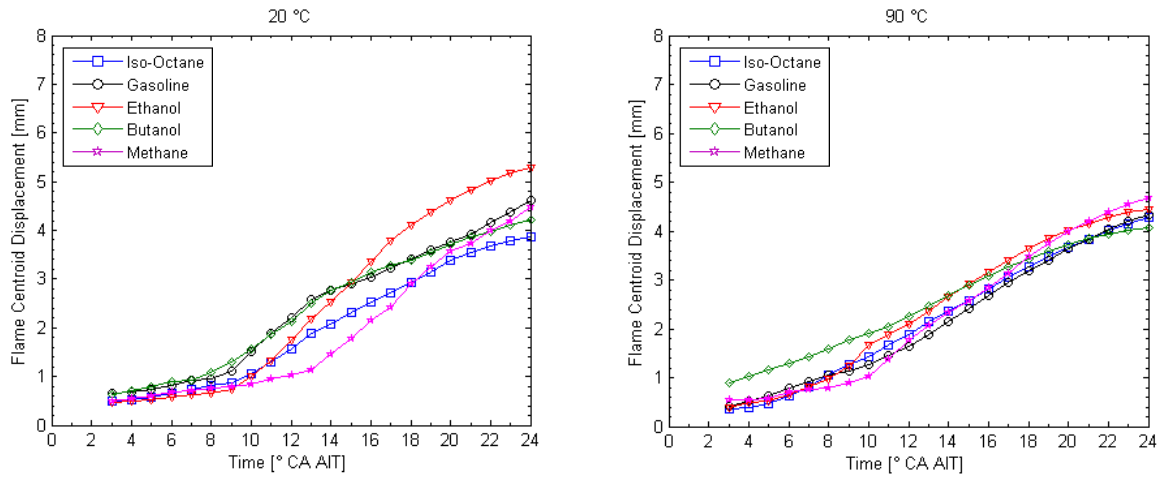
Fig. 16. Cumulative Flame Centroid Path Length; ϕ=1.0, 20 °C and 90 °C.
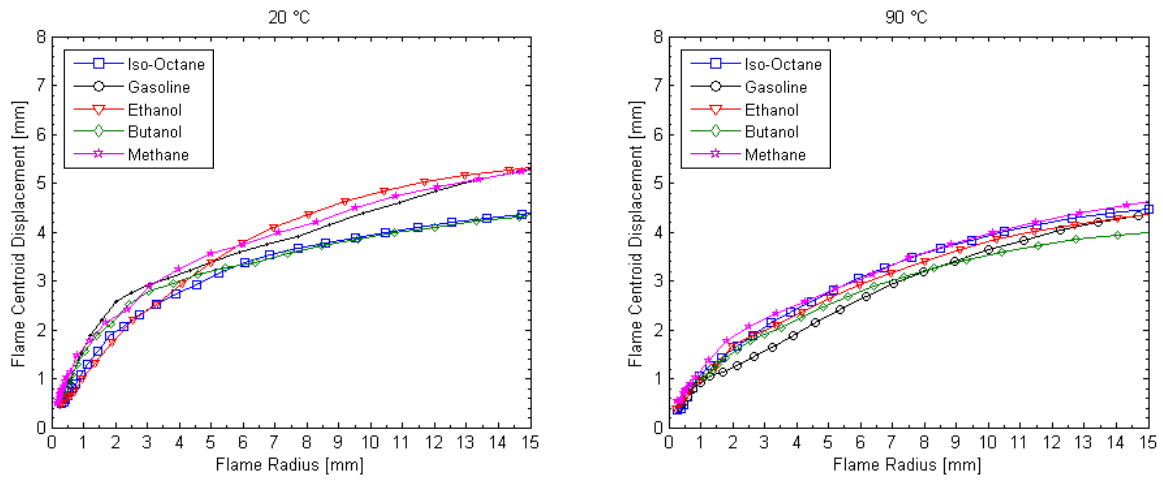
Fig. 17. Cumulative Flame Centroid Path Length Relative to Flame Radius; ϕ=1.0, 20 °C and 90 °C.
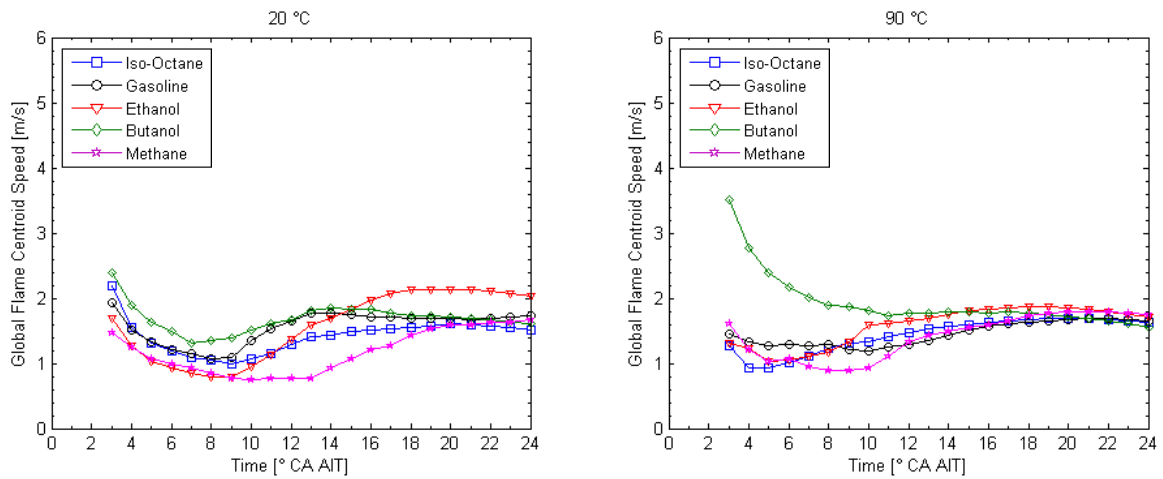
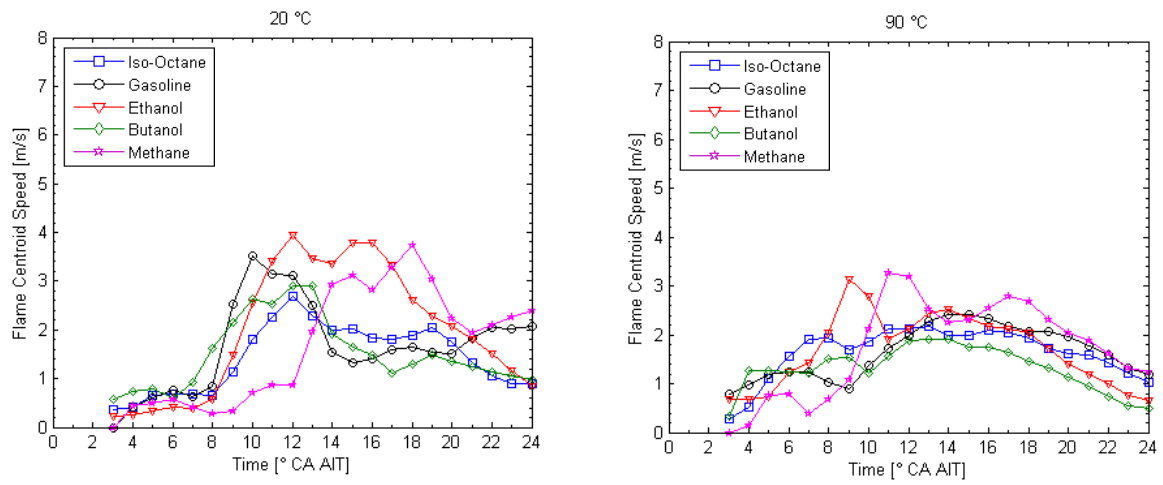
Fig. 18. Global Flame Centroid Speed; ϕ=1.0, 20 °C and 90 °C.

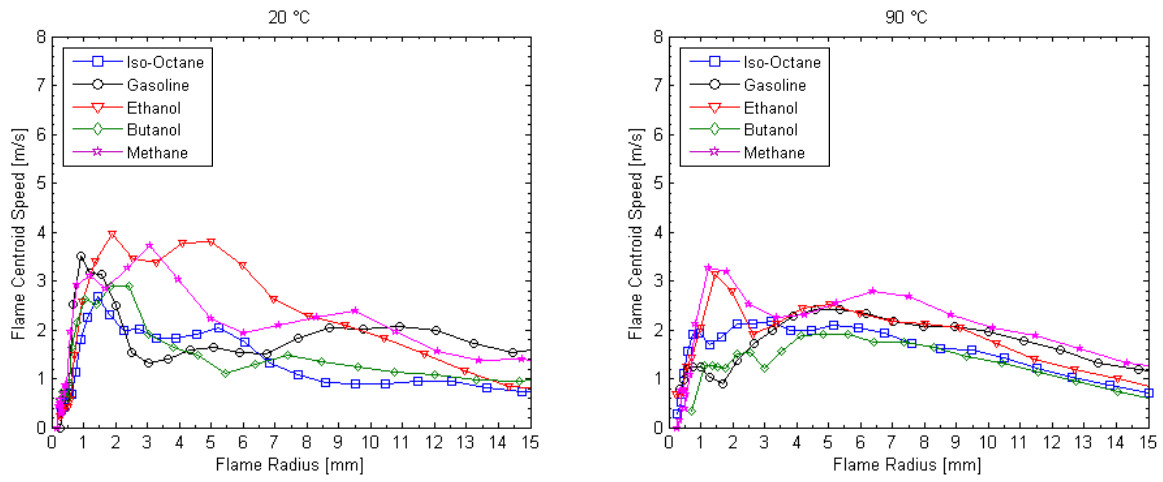**Fig. 19.** Local Flame Centroid Speed; ϕ=1.0, 20 °C and 90 °C.

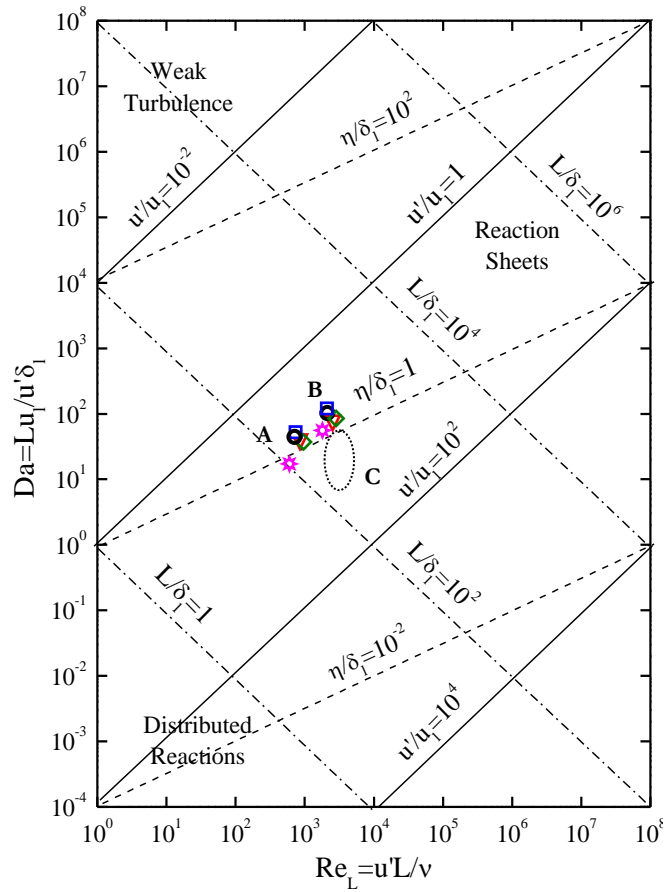**Fig. 20.** Local Flame Centroid Speed Relative to Flame Radius; ϕ=1.0, 20 °C and 90 °C.

Fig. 21. Regimes of Turbulent Premixed Combustion in the Diagram of Abraham *et al.* [69]: Zone A at atmospheric conditions; Zone B at engine ignition timing; Zone C at ignition timing with reduced laminar burning velocity values due to residuals or lean mixtures. Symbols refer to different fuels according to symbols key used everywhere in this paper.
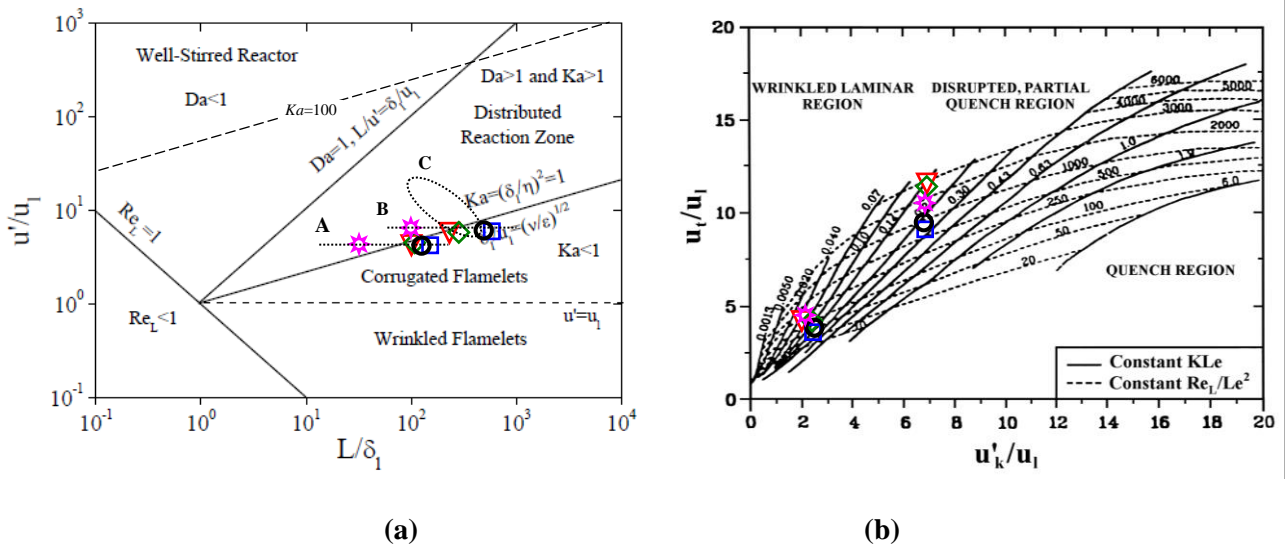

(a)   **(b)**

Fig. 22. Regimes of Turbulent Premixed Combustion. Symbols refer to different fuels at conditions A, B, C, as described in the text: **(a)** Peters [70–71]; **(b)** Bradley [73]. Symbols refer to different fuels according to symbols key used everywhere in this paper.